Research Article

Al Fath Farisy Kusuma Amanta, Teguh Muttaqie*, Aditya Rio Prabowo*, Heru Sukanto, Biatna Dulbert Tampubolon, Quang Thang Do, Branislav Djordjevic, and Seung Jun Baek

Investigating the influence of plate geometry and detonation variations on structural responses under explosion loading: A nonlinear finite-element analysis with sensitivity analysis

https://doi.org/10.1515/cls-2024-0019
received May 04, 2024; accepted October 23, 2024

Abstract: This study presents the results of a numerical analysis of the response of Domex 700 and Dormex 1100 steel plates with varying geometries, combined with several different parameters such as a thickness of up to 6 mm and a trinitrotoluene (TNT) mass. Using ABAQUS software, finite-element analysis was run to examine the structural response ability of the steel plates to explosions. In terms of deformation and energy dissipation, the results showed a large differentiation. A sensitivity analysis was used to examine each simulation result in terms of the structural response performance to explosions and identify the variables that had the greatest impact on variations in the thickness, material, geometry, and TNT mass. The best numerical simulation results were found using the multi-attribute decision-making (MADM) approach. Annotations are utilized to assist in identifying the various modifications made during testing. Annotations LXXI to LVIII achieved the lowest value of 6.176×10^{-09}, signifying the best results according to calculations made using the MADM approach. This is evidenced by the structural events, demonstrating that the deformation, von Mises stress, and energy dissipation in the circular plate structure were not significantly impacted by the explosion. The variables that most significantly affect variations in deformation, von Mises stress, and dissipated energy – variables that significantly impact the structural response to explosions – are identified through the sensitivity analysis approach. The results of this research can be used to optimize the structural response performance of circular plates.

Keywords: explosion, finite-element analysis, structural responses, multi-attribute decision making, sensitive analysis

1 Introduction

Ships have a crucial role in the global economy, facilitating global trade, connecting various ports worldwide, and forming one of the backbones of the goods and people transportation system. Despite the critical role of ships in the movement of the global economy, ship accidents often occur. These pose a severe threat, especially ship accidents due to explosions, which can threaten the safety of the ship's crew and have long-term impacts on the environment. The types of shipping accidents that occurred most frequently in 2021 were collisions (31% of all the accidents reported), fire/explosions (25%), and grounding (20%). The total number of crashes (54) was 34% lower than the 10-year average (2011–2020) of 82, the number of fire/explosion accidents (44) was 23% above the 10-year average of 36, and the number of groundings (36) was 40% below the 10-year average of 60 [1]. This shows that accidents due to explosions were among the most frequent incidents in 2021.

Ship collisions often occur, so it is crucial to conduct analyses of a ship's structure [2]. In previous studies, researchers investigated the response of geometry to variations in the blast

* **Corresponding author: Teguh Muttaqie,** Research Center of Testing Technology and Standard, National Research and Innovation Agency (BRIN), Tangerang, Indonesia, e-mail: teguh.muttaqie@brin.go.id
* **Corresponding author: Aditya Rio Prabowo,** Department of Mechanical Engineering, Universitas Sebelas Maret, Surakarta, Indonesia, e-mail: aditya@ft.uns.ac.id
Al Fath Farisy Kusuma Amanta, Heru Sukanto: Department of Mechanical Engineering, Universitas Sebelas Maret, Surakarta, Indonesia
Biatna Dulbert Tampubolon: Research Center of Testing Technology and Standard, National Research and Innovation Agency (BRIN), Tangerang, Indonesia
Quang Thang Do: Department of Naval Architecture and Ocean Engineering, Nha Trang University, Nha Trang, Vietnam
Branislav Djordjevic: Innovation Center of Faculty of Mechanical Engineering, Belgrade, Serbia
Seung Jun Baek: Advanced-Green Technology Center, Korea Marine Equipment Research Institute, Busan, South Korea

loading of trinitrotoluene (TNT) using the Conventional Weapons Effects Program (CONWEP) method [3–7]. The CONWEP approach, which is based on empirical data on conventional weapons and offers forecasts of blast stress, deformation, and other pertinent aspects, is used to model explosion impacts on structures. In this study, the CONWEP model was employed to predict the structural behavior of an explosion on a circular plate by considering several factors, such as the mass and type of explosive (TNT), the standoff distance, and the ambient conditions. These details demonstrate the validity and reliability of the CONWEP technique for conducting a structural analysis under blast-loading scenarios [8,9].

One study also discussed the energy dissipation obtained from the geometry when it experiences an explosion, while research on the deformation that occurs in specimens has also been carried out using the CONWEP method [10,11]. An analysis of the response of a structure to explosions should be performed in order to mitigate the occurrence of fatal accidents in the event of the structure's inability to withstand the blast loading from an explosion. This research presents the results of a numerical simulation analysis of the circular response of Domex 700 (D700) steel and Domex 1100 (D1100) steel plate structures to varying blast loads. An explosion is an unstable event, in terms of chemistry and energy, that has the potential to cause sudden expansion accompanied by the generation of heat and rapid changes in pressure in a very short time [12]. The plastic deformation of a structure's geometry is influenced by the stress experienced and the amount of energy absorbed due to the explosion [13].

Numerical simulations were carried out with finite elements and ABAQUS, using the CONWEP method to simulate the explosions. Tests were carried out on plates using different thicknesses and geometries to determine the deformation, plastic dissipation energy, and stress resulting from different blast loads. These data can be used for mitigation efforts in case of ship accidents.

2 Literature review

2.1 Shell buckling

In many engineering constructions, plate and shell structures are used as fundamental components. Throughout their service life, these structures are frequently exposed to complicated loading circumstances that might alter their dynamic properties and result in buckling failure [14]. Furthermore, the existence of fractures significantly affects their quality and degrades their performance. Shell buckling can be caused by a number of things, including blast loading. It is believed that structures are prone to compressive stress, which might result in abrupt failure without any prior indication of deformation [15]. Because of the tremendous pressure that a blast wave creates, shell structures are susceptible to collapsing during an explosion, which can degrade or even destroy their structural integrity. The unequal distribution of pressure over the geometry can lead to increased stress at certain areas in a blasted shell structure, which can soon cause the damaged structure, for example, a plate with a stiffener, to buckle. The formula for shell buckling is provided in Eq. (1):

$$\tau_{\text{cr}} = k_v \frac{\pi^2 E}{12(1 - v^2)\left(\frac{h}{t}\right)^2}. \tag{1}$$

The critical shear buckling load is determined by multiplying the critical buckling stress by the web area. The elastic modulus, Poisson's ratio, web depth, and web thickness are represented by the letters E, v, h, and t, respectively. To calculate the shear buckling stress, the shear buckling coefficient (k_v), which varies depending on whether the web is stiffened or not, is also dependent on whether the entire cross-section or only the web is taken into account. When a plate with a long stiffener is subjected to a compressive stress, σ, it will eventually reach the critical stress and cool down. The plate will proceed to the post-bending stage. A feature of plates is that the applied load tends to increase in tandem with the deflection, resulting in stable post-bending. We define this in Eq. (2):

$$\frac{\sigma}{\sigma_{\text{cr}}} = 1 + \frac{3}{8}(1 - v^2)\left(\frac{w}{t}\right)^2, \tag{2}$$

where the buckling deflection's amplitude is indicated by the letter w for a plate thickness deflection of the same magnitude. The design takes into account the effects of imperfections and plasticity along with the post-buckling strength of the plates in the elastic range. Note that the post-buckling strength of plates is limited to thin plates. To specify the non-dimensional parameter of slenderness, the following equation was used:

$$\bar{\lambda}_p = \sqrt{\frac{f_y}{\sigma_{\text{cr}}}} = \frac{1}{\lambda}\sqrt{\frac{12(1 - v^2)}{k}\frac{f_y}{E}}\left(\frac{b}{t}\right), \tag{3}$$

with f_y representing the yield stress of the material. A plate's geometrical slenderness $\left(\frac{b}{t}\right)$ is directly proportional to its non-dimensional slenderness parameter, $\bar{\lambda}_p$. For a narrow plate, $\sigma_{\text{cr}} \ll f_y$ (high λ_p values), whereas for a stocky plate, $\sigma_{\text{cr}} \gg f_y$ (low λ_p values).

2.2 Finite-element analysis (FEA) using the conventional weapons effect method

Through the division of a structure into several small elements, the finite-element method (FEM) may solve a difficult issue [16–18]. As a result, the structural response to various applied-load circumstances may be thoroughly analyzed. When a system is in equilibrium, the total energy in it is equal to the sum of the external potential energy and the strain potential energy. This is the fundamental idea of an FEA's indirect approach to the lowest potential energy. Eqs. (4) and (5) demonstrate the fundamental concept of the FEM.

The total amount of potential energy is expressed as follows:

$$\Pi = \frac{1}{2}\int_{\Omega} \sigma^T \varepsilon \mathrm{d}V - \int_{\Omega} d^T b \mathrm{d}V - \int_{r} d^T q \mathrm{d}S. \tag{4}$$

The total potential energy of the discretized individual element is expressed as follows:

$$\Pi_e = \frac{1}{2}\int_{\Omega_e} u^T (B^T E B)^T u \mathrm{d}V - \int_{\Omega_e} u^T N^T p \mathrm{d}V - \int_{r} u^T N^T q \mathrm{d}S = 0, \tag{5}$$

$$\frac{\partial \Pi_e}{\partial u} = \mathrm{O\ gives}\{F\} = [K]\cdot\{U\}. \tag{6}$$

The above equations explain that a system will reach equilibrium when the total potential energy is at a minimum. [F] is the external force vector applied to the structure, while [K] explains the structure's matrix, and the variable [U] explains the displacement vector. With these, a structure's behavior can be predicted under a load such as pressure or an external force.

An FEA can be used to document a problem in various cases, such as explosions. When an FEA is combined with the CONWEP method, which is used to calculate the effects of explosions based on the distance and mass of the explosives, the CONWEP method serves to provide initial data on the explosion pressure on the structure and is involved in the FEA model regarding the dynamic response of the structure to the explosion. An explosion is a mechanism consisting of the generation of a shock wave that, upon impacting the unexploded material, activates it through a shock pressure force. Materials that explode through explosions are called explosives or high explosives, such as TNT [19]. Both the relationship between the reflected pressure and the incoming shock wave are crucial for understanding and predicting how a blast will affect a structure when employing the CONWEP method [20]. A surface made up of solid or shell elements, or a collection of predetermined segments, is affected by the load. According to Eq. (7), the pressure p acting on a segment takes into account the pressure wave's angle of incidence θ, where p_i is the incident pressure and p_r is the reflected pressure

$$p = p_\mathrm{i}\cdot(1 + \cos\theta - 2\cos^2\theta) + p_\mathrm{r} \cdot 2\cos^2\theta. \tag{7}$$

A complex analysis is needed to determine the equivalent weight of TNT associated with deflagration. Models predicting mid-field deflagration effects are impractical for the characterization of far-field deflagrations and vice versa. Estimations of near-field deflagration effects *via* TNT equivalence methods generally lack accuracy [21–23]. The modified Friedlander Eq. (8) accurately describes the blast pressure–time history at a fixed point:

$$P(t) = P_0 + P_\mathrm{s}\left(1 - \frac{t - t_\mathrm{a}}{t_\mathrm{d}}\right)e^{-b\cdot\frac{t-t_\mathrm{a}}{t_\mathrm{d}}}, \tag{8}$$

where the absolute pressure recorded at the point of interest (time t) following the detonation is represented by $P(t)$, the undisturbed atmospheric pressure is identified by P_0, the peak overpressure is identified by P_s, the blast wave's arrival time at the point of interest is indicated by t_a, the positive phase duration is indicated by t_d, and the decay is represented by the b coefficient. Figure 1 illustrates the conventional curve that Eq. (4) describes.

The pressure–time history is divided into two separate phases, as shown in Figure 1. The positive phase begins at time instant $P(t)$, with a peak overpressure, and rapidly decays to a value below the undisturbed air pressure, which is generally referred to as the negative phase, after the requisite time span for the blast wave to reach the place of interest. The blast force crushes the affected structure during the positive phase, and a reversed blast wind arises during the subsequent negative phase to further impact the target [24].

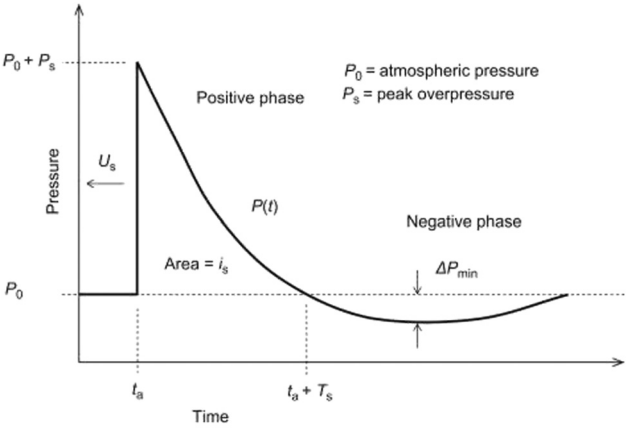

Figure 1: Blast wave pressure–time history (illustration based on the study of Povey [24]).

In recent decades, a number of empirical techniques for characterizing the primary characteristics of the blast wave pressure–time history curve have been developed. A scaling law was introduced to assess the effects of large-scale explosions because tests are typically carried out at small scales. The scaled distance, which connects the explosion's center to a specific point using the energy released by the explosive, is one of the crucial metrics used to assess the effects of an explosion. It serves as a gauge for the explosion's impact on a structure at a given distance. Eq. (9) expresses the scaled distance:

$$Z = \frac{R}{W_{\text{TNT}}^{\frac{1}{3}}}, \tag{9}$$

where R is the place of interest's distance from the explosion site and W_{TNT} is the weight of TNT that was previously introduced. Eq. (7) can be used to analyze the structural response to explosions at various possible scales.

2.3 von Mises stress

von Mises stress is a concept that refers to the internal force generated through external loads applied to an object or structure. Contextually, von Mises stress comes from the distribution force or pressure received by external forces applied to a structure or object. In a structure, a component can receive different forces. Forces with various combinations will cause different stresses at different points, depending on the material and the resulting stress. The normal and shear stress components are contained in a symmetric matrix called the stress matrix, often known as the stress tensor, in three dimensions when it comes to a stress analysis.

In addition, von Mises stress emphasizes giving an important role to the cooling of the structure. The von Mises stress principle is defined in Eqs. (10) and (11).

$$\begin{bmatrix} \sigma_{xx} & \sigma_{xy} & \sigma_{xz} \\ \sigma_{yx} & \sigma_{yy} & \sigma_{yz} \\ \sigma_{zx} & \sigma_{zy} & \sigma_{zz} \end{bmatrix}, \tag{10}$$

$$\begin{bmatrix} \sigma_1 & 0 & 0 \\ 0 & \sigma_2 & 0 \\ 0 & 0 & \sigma_3 \end{bmatrix}. \tag{11}$$

The principal stresses or the stress components represented by the three stress tensors can be used to compute the von Mises stress. For a given stress state, the same von Mises stress, σ_v, can be obtained using either of the formulas in Eqs. (12) and (13).

$$\sigma_v = \sqrt{\frac{(\sigma_{xx} - \sigma_{yy}) + (\sigma_{yy} - \sigma_{zz}) + (\sigma_{zz} - \sigma_{xx}) + 6(\sigma_{xy}^2 + \sigma_{yz}^2 + \sigma_{zx}^2)}{2}}, \tag{12}$$

$$\sigma_v = \sqrt{\frac{(\sigma_1 - \sigma_2)^2 + (\sigma_2 - \sigma_3)^2 + (\sigma_3 - \sigma_1)^2}{2}}. \tag{13}$$

These formulas represent the stress value that results from combining a component's shear and normal stresses at a given position. We can determine the amount of a certain stress, which is crucial for providing strength and preventing material failure, by computing the equivalent stress. von Mises stress frequently employs stress in structural analysis to predict when an object may fail or fail permanently. Furthermore, there is an indirect relationship between the von Mises stress and the occurrence of deflection and dissipation energy [25].

When a structure is shifted or distorted as a result of external loads such as vibration, momentum, or temperature, energy dissipation frequently occurs [26]. Furthermore, in the analysis of a structure, energy dissipation is frequently used for mitigation [27]. Friction between surfaces, material deformation, and energy transmission to the surrounding medium are all factors that contribute to the process of energy dissipation. Therefore, the structural responses to applied stress are evaluated using energy dissipation as a key indication. Eqs. (14) and (15) can be used to define the dissipation energy.

$$\text{ED} = \int_0^{\delta} F(\delta)\text{d}\delta, \tag{14}$$

$$\text{SED} = \frac{\text{ED}}{m}. \tag{15}$$

$F(\delta)$ describes the function of deformation or displacement when force is applied to a structure, ED describes the total energy dissipation, and m is the total mass of the deformed structure. In general, several main mechanisms cause energy dissipation to occur in a system. First, plastic deformation is a process where mechanical energy is used to change the structure of a material so that deformation occurs. Second, friction is a phenomenon when mechanical energy is lost, and two surfaces move against each other. Third, heating is the result of mechanical energy being converted into thermal energy due to friction or deformation.

3 Benchmark particular

Benchmarking in numerical simulations is a validation and verification process that ensures the accuracy of the simulation results by comparing the simulation data with

empirical data. Benchmarking specifically involves testing profiles, results, and mesh convergence studies to verify the accuracy of the simulation results.

3.1 Testing profile

The testing profile comprehensively discusses various aspects of the numerical simulation, ranging from the geometry to boundary conditions. In this study, the geometry used was a sandwich panel measuring 31 mm × 31 mm × 5 mm. The plate stiffener used a tie constraint as a preventive measure to prevent movement between the plate and the honeycomb core [28]. The mesh element used was reduced integration (C3D8R) on the front and back of the plate. Then, S4R elements were used in the sandwich geometry. The load used on the plate was with ENCASTRE, so that it could not move in any direction. The symmetry condition about the *x*-axis (XSYMM) was applied to the plane in the direction of the *y*-axis. In addition, the symmetry condition of the *y*-axis (YSYMM) was applied to the plane parallel to the *x*-axis, as shown in Figure 2.

3.2 Results

The benchmarking results from the CONWEP helped provide essential results in evaluating models for their ability to simulate the effects of TNT explosions with masses of 1, 2, and 3 kg on the structural response that occurs in sandwich panels. This was achieved by involving empirical data from trials carried out in previous studies and comparing them with the current study. The data from the numerical simulation results between the previous and present studies are presented in Table 1.

The results of the numerical simulations carried out in the previous study and present study used the same variations, namely varying the mass of TNT used for the sandwich panels from 1 to 3 kg. The benchmarking results that were carried out with the results of the previous study showed a displacement of 69.19 mm with a TNT mass of 1 kg. At the same mass, the difference in displacement between the previous and present studies was 1.03 mm with an error of 1.4%. The results of the numerical simulations carried out by both studies showed that the mass or load given to the sandwich panel can influence the structural response of the sandwich panel. Contour illustrations of the numerical simulation results of the two studies are shown in Figures 3 and 4.

3.3 Mesh convergence study

Mesh convergence is one of the crucial components in an FEA when the convergence value can reach the actual solution. It involves combining the elements in the geometry and analyzing the impact of the process on the accuracy of the results or the achievement of stability (convergence). At this stage, further changes no longer significantly impact the results, so determining the optimal element size is very important in order to obtain accurate results [29]. In this study, a mesh element size of 6 was used because the mesh reached a convergence or stability value, so at this value, the mesh convergence showed the achievement when the simulation results were no longer affected by the level of mesh

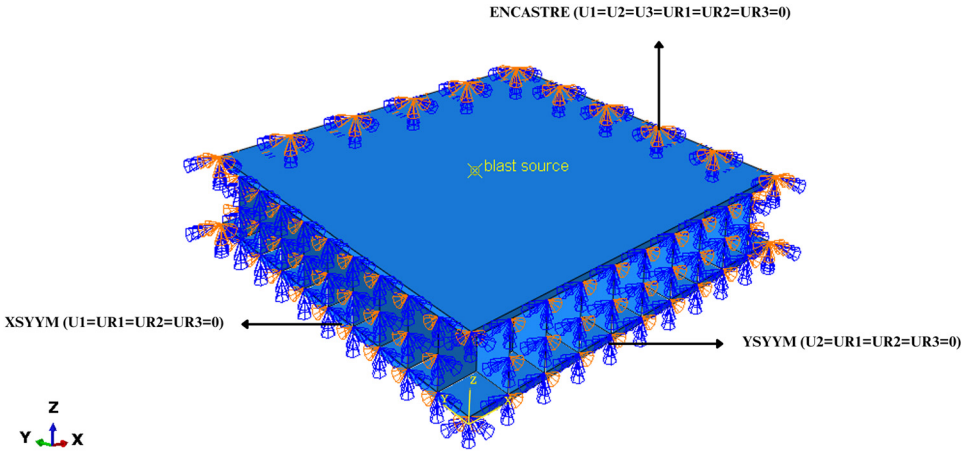

Figure 2: Sandwich panel boundary condition.

Table 1: Data from numerical simulation results of the previous study and the present study

Mass of TNT	Displacement (mm)		Error (%)	
	Numerical result (*previous study*)	Numerical result (*present study*)	*Previous study*	*Present study*
1 kg	69.19	70.22	1.4	1.4
2 kg	110.5	110.5	0	0
3 kg	141	143	1.4	1.4
	Average error		0.93	0.93

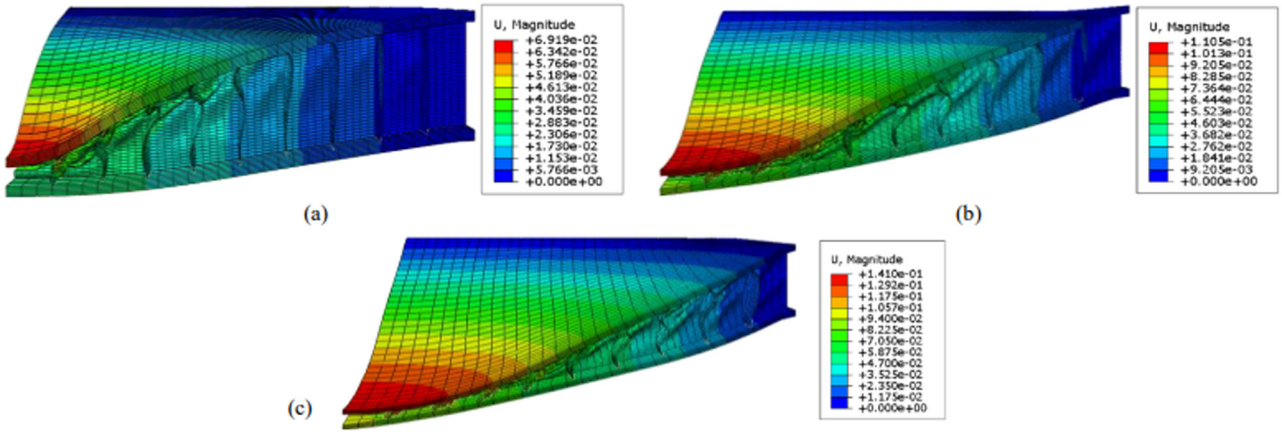

Figure 3: Deflection in sandwich panels with a TNT mass of (a) 1 kg, bar 3; (b) 2 kg; and (c) 3 kg in the previous study.

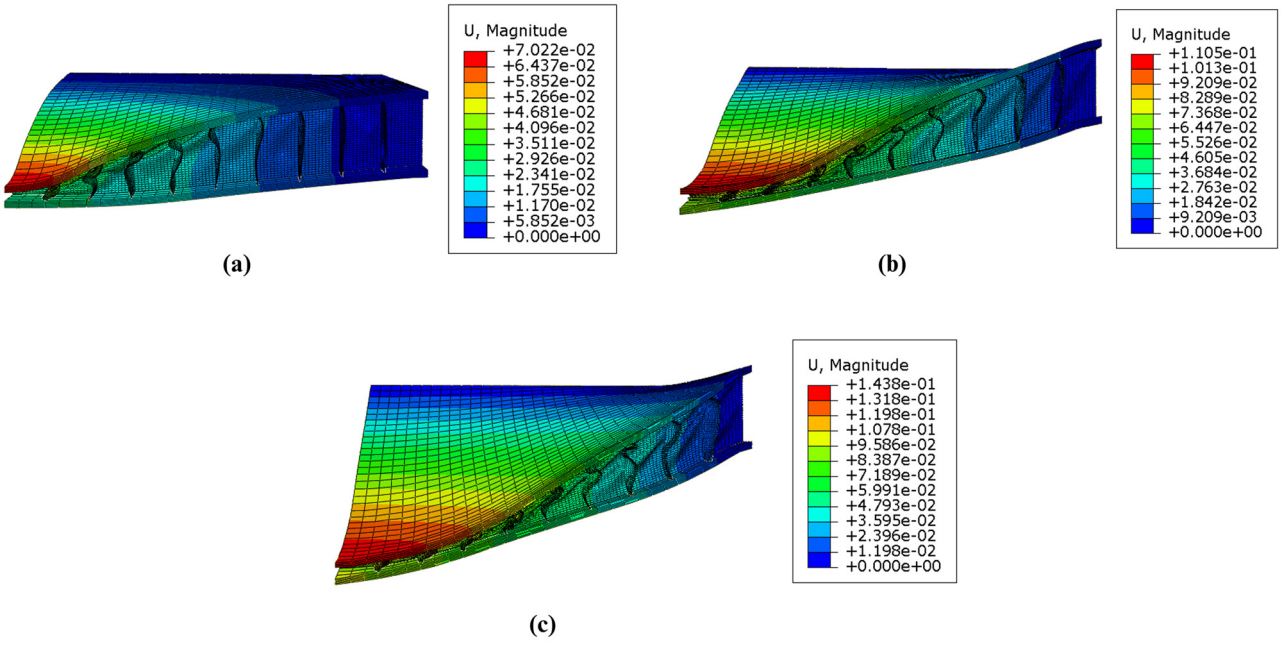

Figure 4: Deflection in sandwich panels with a TNT mass of (a) 1 kg, bar 3; (b) 2 kg; and (c) 3 kg in the present study.

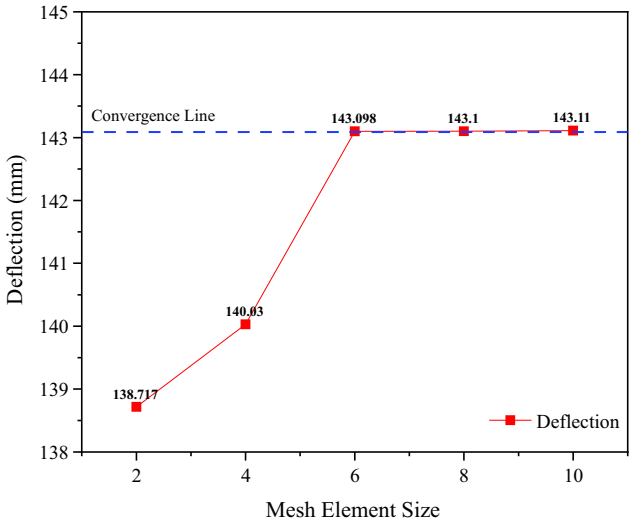

Figure 5: Mesh convergence graph.

fineness used. This is shown in the mesh convergence graph in Figure 5.

4 Methodology

This study used the CONWEP method, which includes software designed to model the effects of explosions and impacts caused by conventional weapons or explosives. CONWEP helps in understanding and predicting the impact of damage that may occur to structures due to explosions. A structural response analysis was facilitated using the FEM and the multi-attribute decision-making (MADM) method to show the best simulation data results with several variations to the geometric structure. A numerical approach was used to solve partial differential equations that described the structural behavior. In the context of a blast analysis or the structural dynamics, FEMs can be used to model the response of structures to blast loads.

4.1 Geometrical model

This study used five types of circular plate geometries: no stiffener, one stiffener, one cross-stiffener, two stiffeners, and two cross-stiffeners. The plate was modeled by representing it as a component in the form of a circle with a radius of 73 mm, whereas the open area had a radius of 53 mm. The S4R shell element was used for this representation. An additional radius of 20 mm served to delineate the clamping area. The test plate was designated as a 'shell revolve' component, with a specific section thickness of 2 mm or 3 mm using a 1.3 mm mesh, as shown in Figure 6.

The clamp was modeled as a 3D "analytical rigid body" with a revolved cross-section shell. It was designed as a holder for the test plate to simulate the boundary conditions used in this experiment. The clamp was given a clamping surface, which limited the clamp area that interacted with the test plate. Figure 7 illustrates the 3D models of various geometric variations.

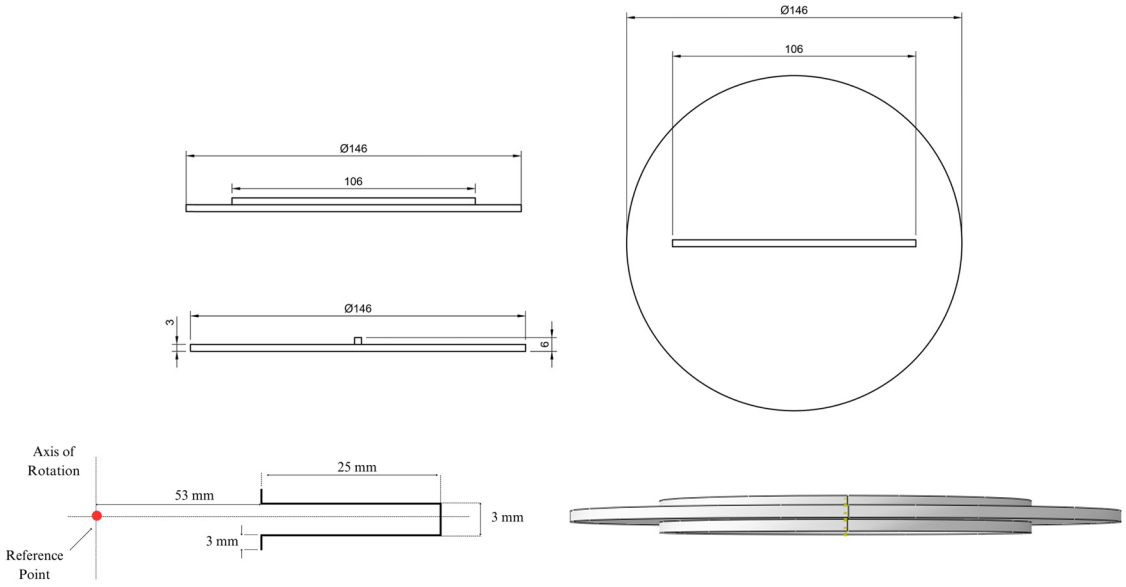

Figure 6: A 2D model of the circular plate geometry.

4.2 Applied material

The Johnson–Cook material model is often used in numerical simulation analyses to describe the response of a material to the geometry of complex mechanical loads. The Johnson–Cook model uses three main parameters for materials: the strain hardening rate, thermal parameters, and strength. These parameters can help accurately describe a material's response to varying conditions and loads. This study applied the Johnson–Cook model to two types of materials: Domex 700 steel and Domex 1100 steel. Domex 700 steel, with a thermal conductivity (m) of 500 and a melting temperature (T_{melt}) of 1,370 K, has been effectively used in previous research, such as in the study by Yuen *et al.* [30]. Similarly, 1100 (D1100) steel, with a thermal conductivity (m) of 1.03 and a melting temperature (T_{melt}) of 1,795 K, has shown promise in research, such as in the work by Pratomo *et al.* [31]. The Johnson–Cook relation, as expressed in Eqs. (16) and (17), was instrumental in capturing the material behavior in these loading scenarios, demonstrating its practical application in real-world situations.

$$\bar{\sigma} = [A + B(\bar{\varepsilon}^{pl})^n]\left[1 + C \ln\left(\frac{\dot{\varepsilon}_{pl}}{\dot{\varepsilon}_o}\right)\right](1 - \hat{\theta}^m), \tag{16}$$

$$\bar{\sigma} = \left[\left(\frac{T - 300K}{T_{\text{melt}} - 300K}\right)\right]. \tag{17}$$

Here,

$$\hat{\theta} = \begin{cases} 0 & T < T_{0,} \\ (T - T_{\text{melt}})/(T_{\text{melt}} - T_0) & T_0 \le T \le T_{\text{melt}}. \\ 1 & T > T_{\text{melt}}. \end{cases} \tag{18}$$

Before considering the standards for Domex 700 steel and 1100 steel, it is necessary to define the chemical composition of the steel, as shown in Tables 2 and 3. These two types of steel have different composition types and percentages. The mechanical property parameters are also different for Domex 700 (a yield strength of 700 N/m 1100 steel and a tensile strength of 750–950 N/m 1100 steel) and circular plate steel Domex 1100 (a yield strength of 1,100 N/m 1100 steel and a tensile strength of 1,250–1,550 N/m 1100 steel). The steel structure standards for ships generally use the ASTM A 131 M standard, which covers structural steel forms, plates, bars, and rivets. Materials with specifications in ASTM A 131 M are divided into two categories: ordinary strength – Classes A, B, D, DS, CS, and E, with a specified minimum melting point of 235 MPa – and higher strength – Classes AH, DH, and EH, with the minimum melting point determined as 315 MPa or 350 MPa.

Under standard test parameters, different references were also used; for Domex 700, EN-10149-2 [32], the European standard for hot-rolled flat products made of high-yield-strength thermo-mechanically rolled steels for cold forming was used, and the impact strength test used the Charpy *V*-test. Notching was carried out in accordance with EN 10045-1 [33]. Meanwhile, for Domex 1100 circular steel, the tensile test was performed according to EN 10002-1 [34] and the impact strength test also used EN 10045-1 [33].

The corresponding constants used to describe a complex material response are comprehensively detailed in

Table 2: Chemical composition percentage of Domex 700 Steel (D700)

	Composition percentage (%)								
Material	**C**	**Si**	**Mn**	**P**	**S**	**Al**	**Nb**	**V**	**Ti**
D700	0.12	0.1	2.1	0.025	0.01	0.015	0.9	0.2	0.15

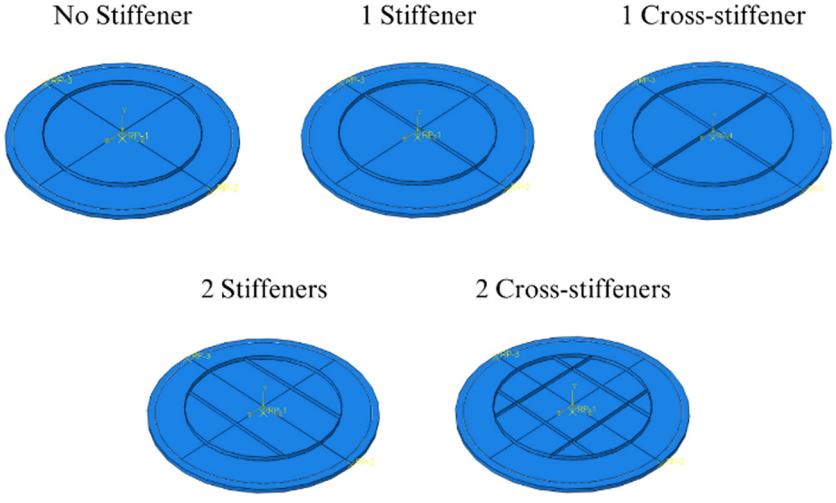

Figure 7: The 3D models of geometry variations.

Table 3: Chemical composition percentage of Domex 1100 Steel (D1100)

	Composition percentage (%)														
Material	**C**	**Si**	**Mn**	**P**	**S**	**B**	**Nb**	**Cr**	**V**	**Cu**	**Ti**	**Al**	**Mo**	**N**	**Ni**
D1100	0.21	0.5	1.4	0.02	0.01	0.04	0.04	0.08	0.08	0.3	0.02	0.02	0.7	0.15	3

Table 4. They ensure a comprehensive understanding of a material's dynamic response to local blast-loading conditions. This approach accurately represents the material behavior of Domex 700 steel and Domex 1100 steel in a given context, as demonstrated in this study.

4.3 Finite-element settings

Boundary conditions, the mesh, and the scenario design are three aspects that are quite important in the numerical simulation process. Boundary conditions are used to regulate system behavior within predetermined boundaries. In contrast, the mesh divides the geometric domain into elements for the numerical simulation. Meanwhile, the scenario list is a series of scenarios or conditions planned using code to make it easier to identify simulation results from different variations. By paying attention to these three aspects, the simulations can be made more accurate and relevant for analyzing the responses to various predetermined situations and conditions.

4.3.1 Mesh configuration

In numerical simulations, the meshing process is the first step and is crucial in providing accurate results. Dividing the meshing elements into more minor elements allows for a simpler representation of complex geometries. Meshing has a vital role in determining the accuracy and reliability of the simulation results, so the choice of mesh type, mesh size, and mesh production are important factors that can influence the quality of the resulting simulation model. In addition, the meshing of the geometry has an important role in the simulation efficiency, because the efficiency depends on the quality of the mesh [35,36]. The mesh in this study used S4R mesh shell elements with a size of 1.3 mm. The number of elements used in the test plate affected the pressure distribution on the test plate as a whole. The mesh applied used a global size of 1.3 mm and had 11,727 total elements. It was chosen because this mesh size achieved convergence or stability in the numerical simulation results. A mesh illustration is shown in Figure 8.

4.3.2 Boundary conditions

Boundary conditions are an important component in preparing numerical simulations; they are parameters that determine the behavior of the system at the boundaries in a numerical simulation. This is quite crucial, because it allows the user to simulate situations according to the actual physical conditions of the object being tested. Boundary conditions include external forces applied to a bounded structure or boundary, as they can influence the results [37]. When appropriate boundary conditions are set, the simulation results can provide more accurate results regarding the structure's response to the environment and the load conditions that are determined. The boundary conditions must be carefully determined, and the actual physical conditions must be considered along with the analysis objectives [38].

The investigation of the structural response of Domex 700 steel and Domex 1100 (D1100) steel circular plates used the ABAQUS approach with the CONWEP approach. The clamping mechanism was assigned a defined clamping surface, representing the region where the mechanism engaged with the test plate. Next, a reference point with certain zero-velocity boundary conditions (X, Y, Z) was established on the clamp, ensuring its stability in space during plate loading, as shown in Figure 9.

The numerical model was subjected to blast loading using the CONWEP interaction, defined as the interaction of the

Table 4: Domex 700 steel and Domex 1100 steel material properties

Material	***A* (MPa)**	***B* (MPa)**	***n***	**ε_0 (s)**	***C***	***m***	**T_{melt} (K)**	**Specific heat (J/kg K)**	**ρ (kg/m^3)**
Domex 700 steel	750	270.6	0.263	0.001	0.014	1.03	1,795	477	7,800
Domex 1100 steel	1,000	490	0.26	0.001	0.001	1.03	1,370	500	7,830

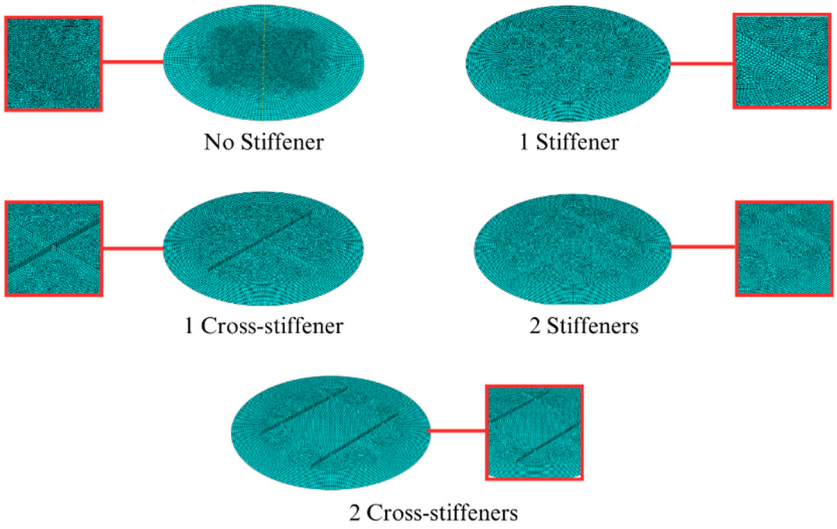

Figure 8: Mesh illustration for geometry variations.

incident wave with the blast area on the test plate. The explosion source was determined at a normal distance of 150 mm from the explosion area. The CONWEP interaction characteristic was defined as an air blast with a mass equivalent to TNT for each specific charge mass ranging from 10 to 40 g.

4.3.3 Scenario list

The scenario list is a collection of various scenarios or conditions that were planned before the simulation was carried out. This can help identify and monitor the simulation results produced from various numerical simulations. Using a list of scenarios makes it easier to compare each scenario's simulation results to understand the impact of the various factors being analyzed better. The scenario list is presented in Tables 5 and 6.

The combination of the plate thickness and the blast mass was used to evaluate diverse scenarios of the structural response to extreme conditions. In order to examine the impact of the thickness on the plate's resistance to blast loads, which has a direct bearing on the structural strength and energy dissipation capacity, plates with thicknesses varying between 2 and 5 mm were chosen [39]. In general, thicker plates can tolerate more plastic deformation, which increases their resistance to buckling and the structure's failure under blast stresses. In this investigation, explosive masses ranging from 10 to 40 g of TNT were used. When deciding how strong of a blast to apply to the plate, the explosive mass was a crucial factor. Greater pressure waves generated by larger blast loads increase the likelihood of plate structure failure or deformation [40].

After numerous simulations with different variants *versus* circular plates, the notation used in Table 5 came to 71. Additionally, the different codes utilized in the list of numerical simulation scenarios made it easier to identify the different types of materials, thicknesses, TNT masses, and geometry modifications that were employed in the numerical simulations. A number of scenarios in different combinations were created to aid in the investigation of

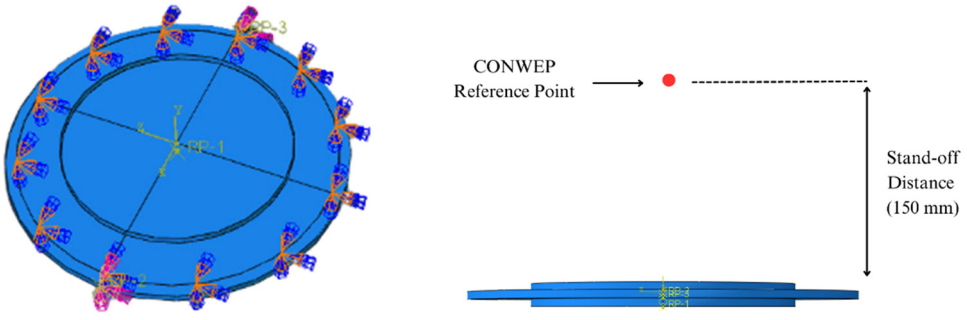

Figure 9: Illustration of boundary conditions on a circular plate.

Table 5: List of numerical simulation scenarios with different variations

Mass of TNT	Geometry	Thickness	Material	Notation
m5	G1	t1	Domex 700 steel	I
m5	G1	t2	Domex 700 steel	II
m5	G1	t3	Domex 700 steel	III
m5	G1	t4	Domex 700 steel	IV
m5	G1	t5	Domex 700 steel	V
m5	G1	t1	1100 steel	VI
m5	G1	t2	1100 steel	VII
m5	G1	t3	1100 steel	VIII
m5	G1	t4	1100 steel	IX
m5	G1	t5	1100 steel	X
m1	G1	t2	Domex 700 steel	XI
m2	G1	t2	Domex 700 steel	XII
m4	G1	t2	Domex 700 steel	XIII
m5	G1	t2	Domex 700 steel	XIV
m6	G1	t2	Domex 700 steel	XV
m7	G1	t2	Domex 700 steel	XVI
m1	G1	t2	1100 steel	XVII
m2	G1	t2	1100 steel	XVIII
m4	G1	t2	1100 steel	XIX
m5	G1	t2	1100 steel	XX
m6	G1	t2	1100 steel	XXI
m7	G1	t2	1100 steel	XXII
m1	G2	t2	Domex 700 steel	XXIII
m2	G2	t2	Domex 700 steel	XXIV
m3	G2	t2	Domex 700 steel	XXV
m4	G2	t2	Domex 700 steel	XXVI
m5	G2	t2	Domex 700 steel	XXVII
m6	G2	t2	Domex 700 steel	XXVIII
m7	G2	t2	Domex 700 steel	XXIX
m1	G2	t2	1100 steel	XXX
m2	G2	t2	1100 steel	XXXI
m3	G2	t2	1100 steel	XXXII
m4	G2	t2	1100 steel	XXXIII
m5	G2	t2	1100 steel	XXXIV
m6	G2	t2	1100 steel	XXXV
m7	G2	t2	1100 steel	XXXVI
m1	G3	t2	Domex 700 steel	XXXVII
m2	G3	t2	Domex 700 steel	XXXVIII
m3	G3	t2	Domex 700 steel	XXXIX
m4	G3	t2	Domex 700 steel	XL
m5	G3	t2	Domex 700 steel	XLI
m6	G3	t2	Domex 700 steel	XLII
m7	G3	t2	Domex 700 steel	XLIII
m1	G3	t2	1100 steel	XLIV
m2	G3	t2	1100 steel	XLV
m3	G3	t2	1100 steel	XLVI
m4	G3	t2	1100 steel	XLVII
m5	G3	t2	1100 steel	XLVIII
m6	G3	t2	1100 steel	XLIX
m7	G3	t2	1100 steel	L
m1	G4	t2	Domex 700 steel	LI
m2	G4	t2	Domex 700 steel	LII
m3	G4	t2	Domex 700 steel	LIII
m4	G4	t2	Domex 700 steel	LIV
m5	G4	t2	Domex 700 steel	LV
m6	G4	t2	Domex 700 steel	LVI

(Continued)

Table 5: *Continued*

Mass of TNT	Geometry	Thickness	Material	Notation
m7	G4	t2	Domex 700 steel	LVII
m1	G5	t2	Domex 700 steel	LVIII
m2	G5	t2	Domex 700 steel	LIX
m3	G5	t2	Domex 700 steel	LX
m4	G5	t2	Domex 700 steel	LXI
m5	G5	t2	Domex 700 steel	LXII
m6	G5	t2	Domex 700 steel	LXIII
m7	G5	t2	Domex 700 steel	LXIV
m1	G5	t2	1100 steel	LXV
m2	G5	t2	1100 steel	LXVI
m3	G5	t2	1100 steel	LXVII
m4	G5	t2	1100 steel	LXVIII
m5	G5	t2	1100 steel	LXIX
m6	G5	t2	1100 steel	LXX
m7	G5	t2	1100 steel	LXXI

Table 6: Coded list of scenarios with different variations

	Code	
Thickness	t1	2 mm
	t2	3 mm
	t3	4 mm
	t4	5 mm
	t5	6 mm
Mass of TNT	m1	10 g
	m2	15 g
	m3	20 g
	m4	25 g
	m5	30 g
	m6	35 g
	m7	40 g
Geometry	G1	No stiffener
	G2	1 Stiffener
	G3	1 Cross-stiffener
	G4	2 Stiffeners
	G5	2 Cross-stiffeners

the circular plate's structural response to an explosion. By using this approach, the modeling allowed for more accurate results through the analysis of diverse combinations.

4.4 MADM method

MADM is an analytical approach used to make complex decisions by considering several relevant alternative criteria or attributes [41–48]. By using the MADM method, decision makers can evaluate and compare various alternatives based on different criteria (such as crashworthiness, fire safety, *etc.*), making it possible to obtain results that are in accordance with the objectives [49–56].

The simple addition weighted (SAW) method is one type of the MADM method that is used to weight the values obtained for each criterion. The SAW method is quite commonly used. It determines the performance weight for each alternative owned by each attribute. This method requires a data normalization process and compares the data with all the result rankings. Data normalization is shown in Eq. (19), and the value of each alternative is calculated using Eq. (20).

$$r_{ij} = \begin{cases} \dfrac{x_{ij}}{\mathrm{Max}_i x_{ij}} \text{Maximum Criteria Value} \\ \dfrac{\mathrm{Min}_i x_{ij}}{x_{ij}} \text{Minimum Criteria Value,} \end{cases} \tag{19}$$

$$v_i = \sum_{j=1}^{n} w_r r_{ij}. \tag{20}$$

The calculation model using MADM is explained by the equation. The matrix's alternative values and criteria are described by x_{ij}, and their relationships are established by $\mathrm{Max}_i x_{ij}$, which specifies the maximum value of each alternative and criterion. Next, w_r describes the assigned weight value and r_{ij} defines the matrix normalization so that v_i, the defined alternative's final value, may be obtained.

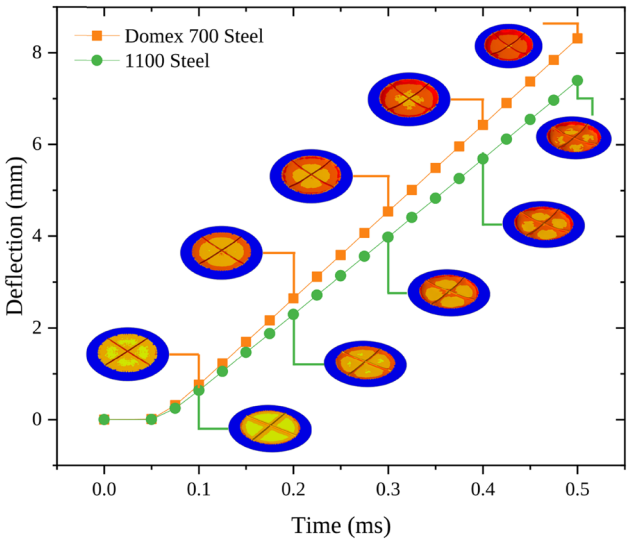

Figure 10: Deflection graph of Domex 700 steel and 1100 steel.

5 Results and discussion

5.1 Results based on material variation

The simulation carried out on the geometry used several variations, one of which was a variation in the material between Domex 700 (D700) steel and 1100 (D1100) steel, as shown in Table 4. The data from the CONWEP simulation results with a TNT mass of 30 g showed that the geometry with the Domex 700 (D700) steel material produced a more significant deflection compared to the Domex 1100 (D1100) steel material, with a difference of 0.92 mm at 0.5 ms. The data are presented in Figure 10.

The graph in Figure 11 shows that Domex 700 (D700) steel experienced a more significant deflection compared to 1100 (D1100) steel. The difference in the deflection values for the two different materials was analyzed through the

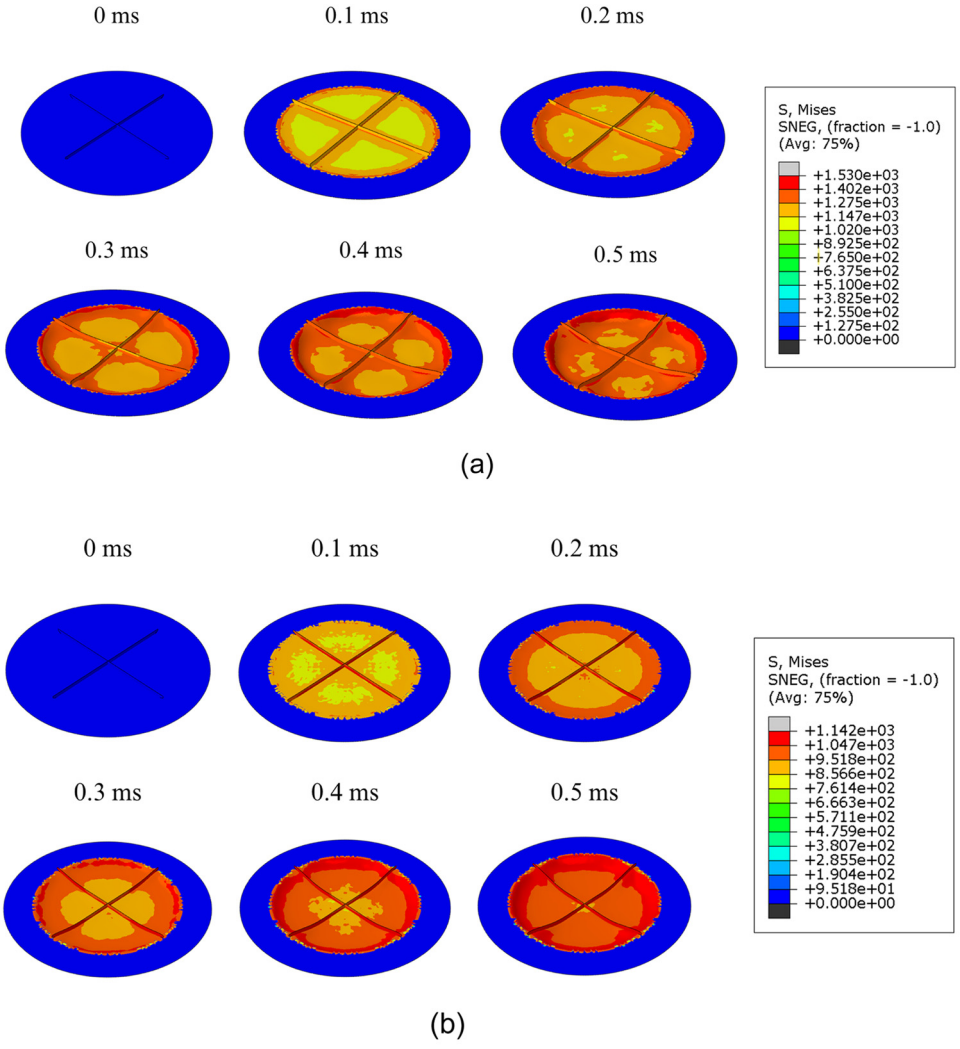

Figure 11: von Mises stress contour, one cross-stiffener: (a) Domex 700 steel and (b) 1100 steel.

stress value produced by the geometry. The geometry with the Domex 700 (D700) steel material received a greater von Mises stress than 1100 (D1100) steel, with a difference in the value of 388 Pa. Therefore, the force distribution produced by Domex 700 (D700) steel was more significant, so the energy absorbed by the material was relatively high. This resulted in the deflection being greater than that of 1100 steel. The difference in the deflection values between the two materials was influenced by the ability of each material to accept the force obtained from the explosion on the geometry. This shows the significant influence of the explosion on the geometric response of different materials, where the energy absorbed increases with increasing time until it reaches the maximum stress and energy dissipation values, as illustrated in Figures 11 and 12.

5.2 Results based on thickness variation

Thickness variations in structures can significantly impact the structural response to explosions. Varying the thickness of a structure can cause a different stress distribution when the structure is exposed to an explosion. An analysis of varying thicknesses can help determine the structural behavior in response to blast loads. In the numerical

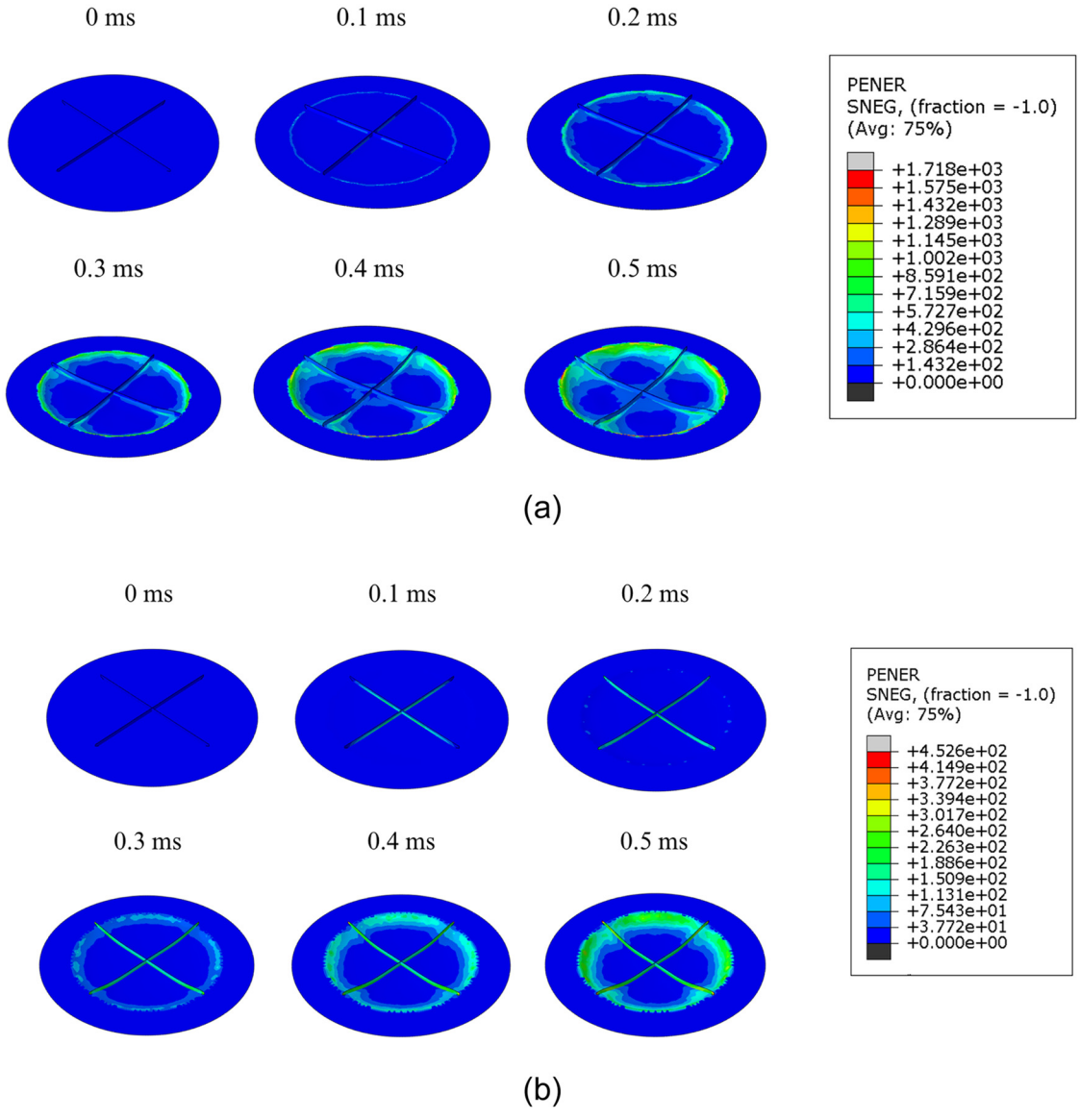

Figure 12: Energy dissipation contour, one cross-stiffener: (a) Domex 700 steel and (b) 1100 steel.

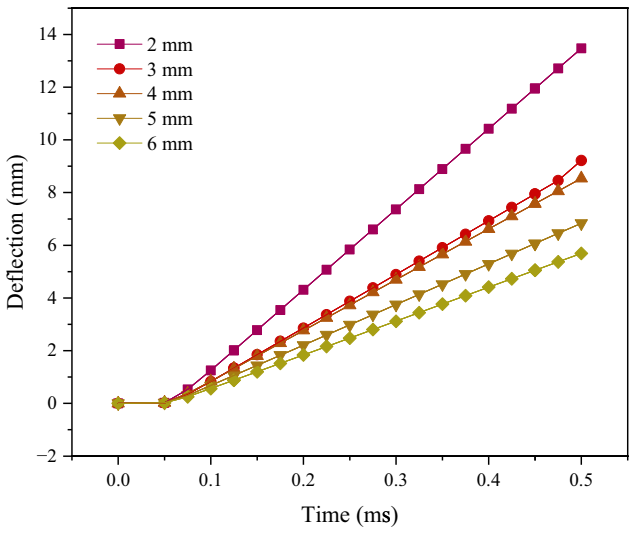

Figure 13: Deflection graph with thickness variations.

simulation, thicknesses ranging from 2 to 6 mm were used with the same blast load mass of 30 g. Data on the effects of the explosions on geometries with varying thicknesses are presented in Figure 13.

The data resulting from deflections that occurred at varying thicknesses showed that the geometry's thickness significantly influenced the explosion. The largest deflection was obtained at a thickness of 2 mm, with a deflection of 13.47 mm, and the slightest deflection occurred at a thickness of 6 mm, with a deflection of 5.69 mm. As the thickness increased, the resulting deflection became smaller compared to the thickness, which tended to be small. Thus, there was a correlation between the thickness of the material and the level of deformation that occurred due to the explosion. Therefore, the ability of a given thickness to withstand the forces received from an explosion influences the structural response of the geometry.

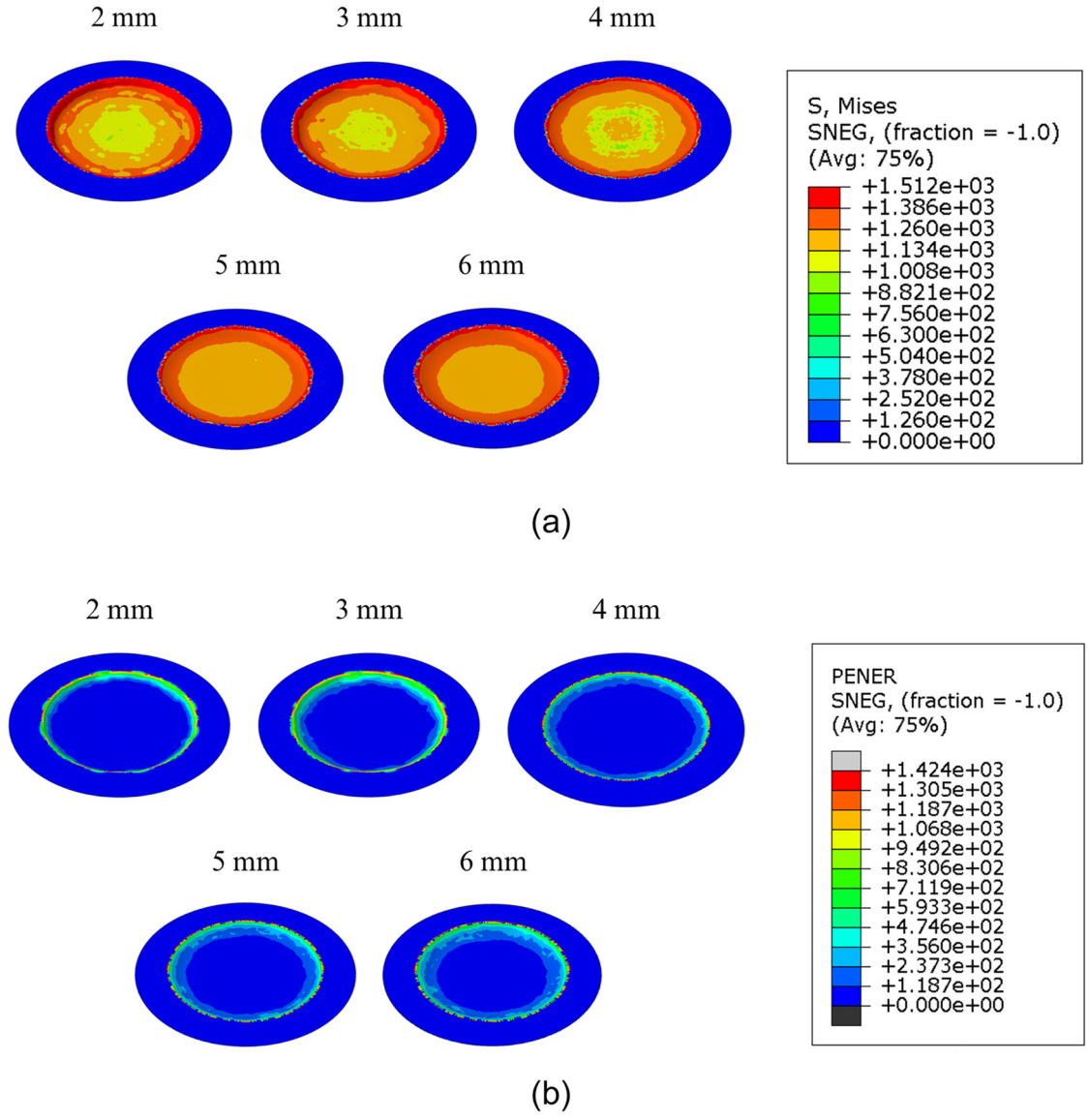

Figure 14: (a) von Mises stress and (b) energy dissipation contour for a circular plate with thickness variations.

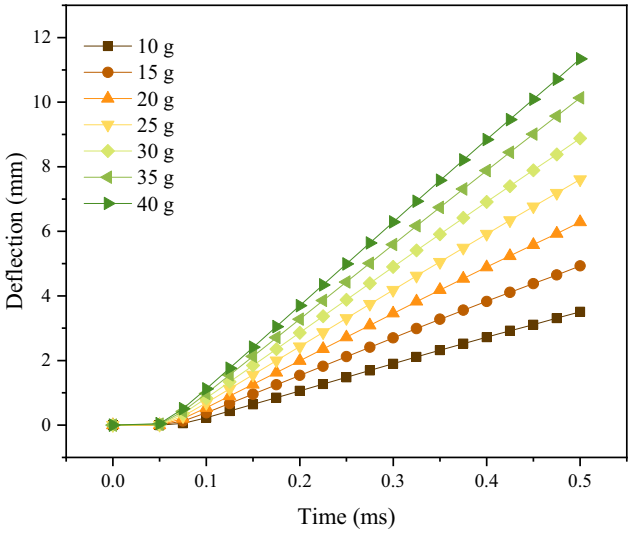

Figure 15: Deflection graph with varying masses of TNT.

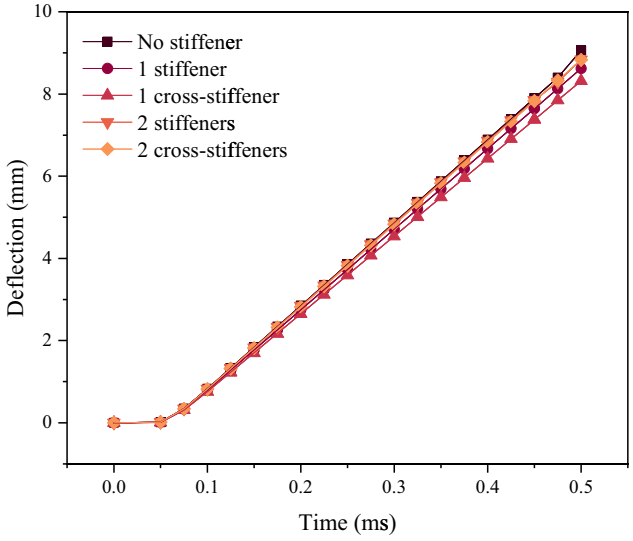

Figure 17: Deflection graph based on geometry variations.

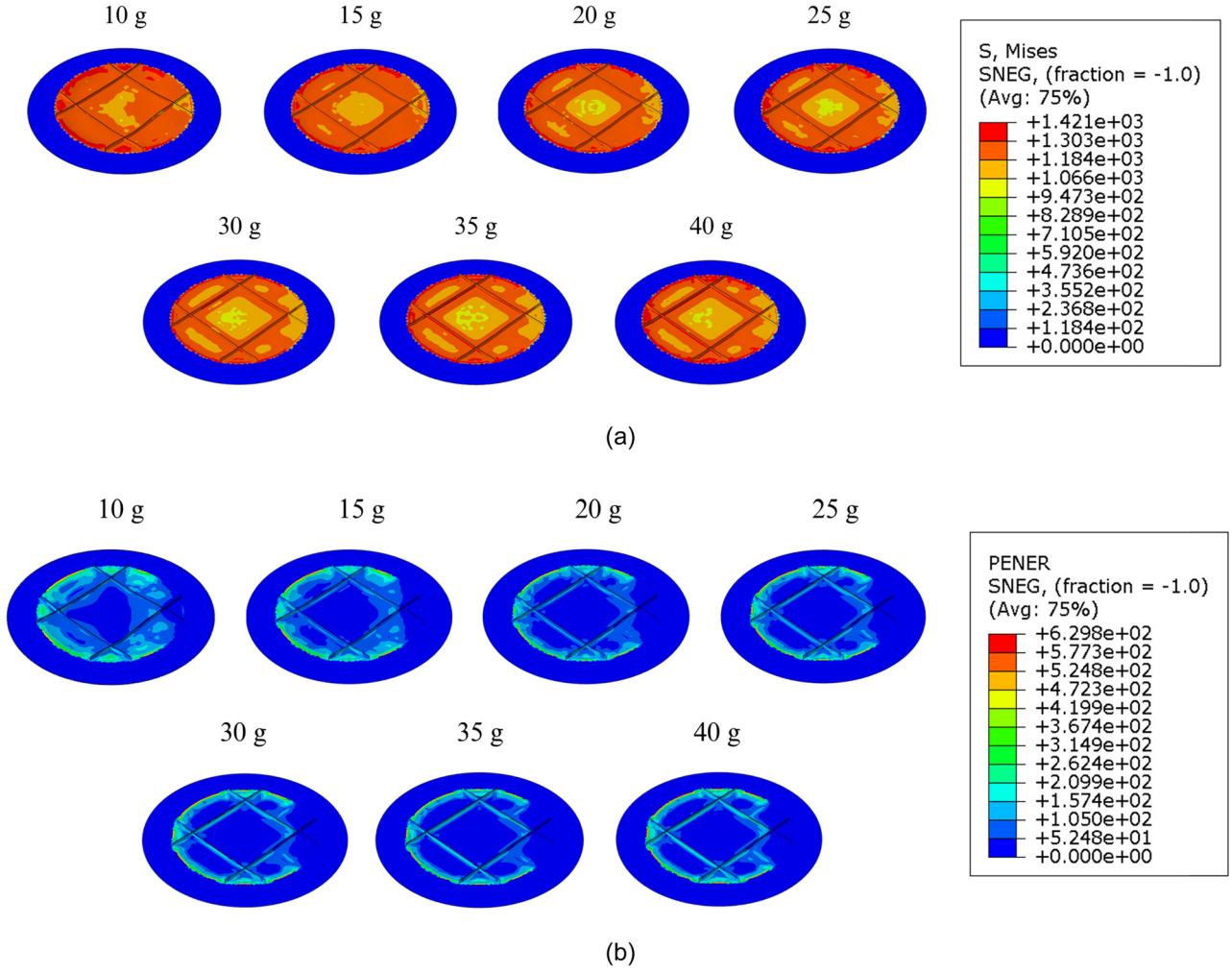

Figure 16: (a) von Mises stress and (b) energy dissipation contour for a circular plate with a varying mass of TNT.

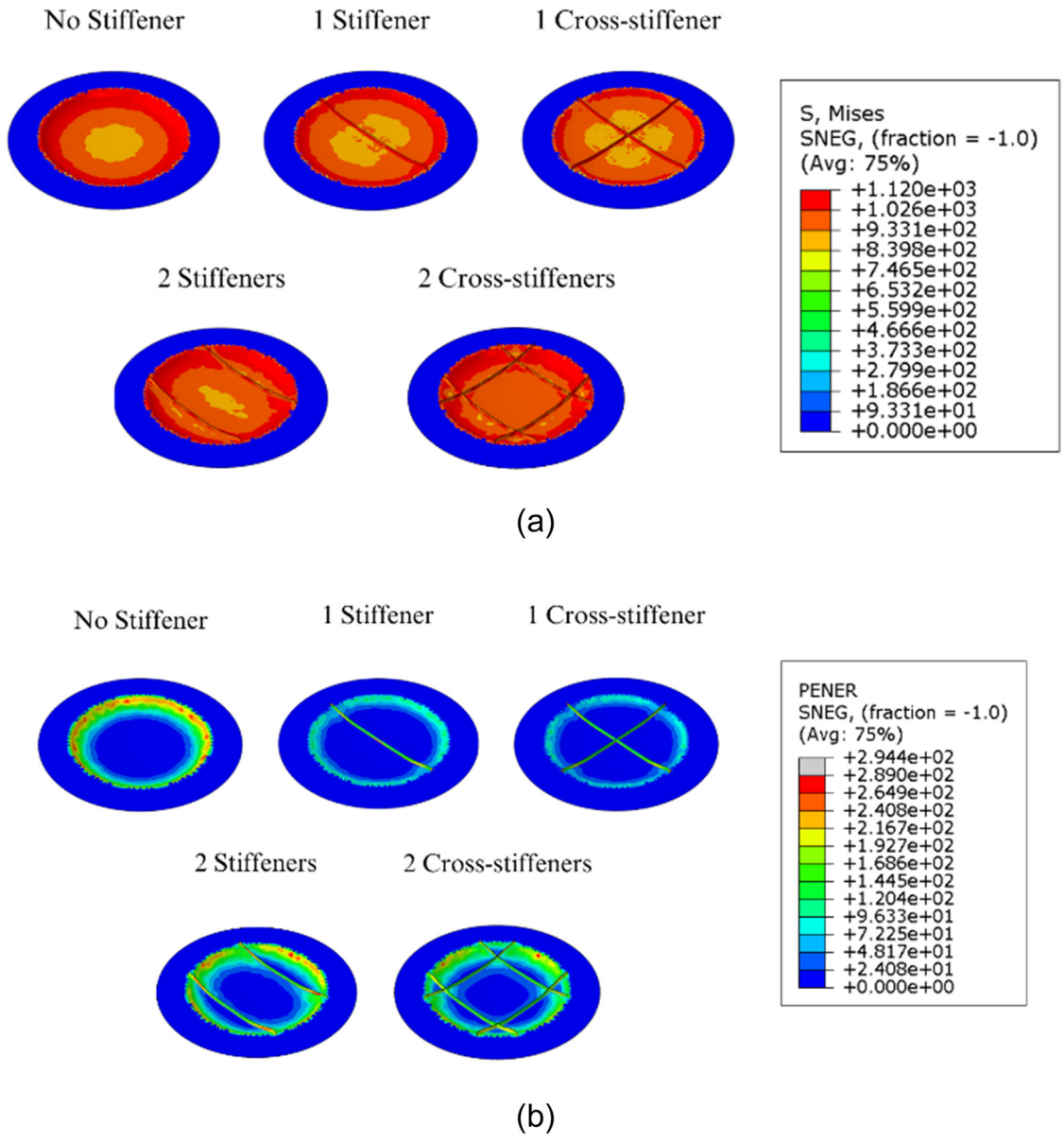

Figure 18: (a) von Mises stress and (b) energy dissipation contour for a circular plate with geometry variations.

Deformations in geometries with varying thicknesses can occur because there is stress received by the geometry, resulting in dissipated energy, which is absorbed by the geometry and produces deflection. The impact of this dissipated energy is then reflected in the form of deformation that occurs in the geometry. The factors that differentiate each thickness are the von Mises stress value obtained and the energy produced by the von Mises stress on the geometry, which are very important parameters. This causes each thickness to have different characteristics when responding to explosions and different abilities to receive force and absorb energy, resulting in different deflections from each thickness. This is shown by different structural responses with the same von Mises stress and energy dissipation values at each thickness, as illustrated in Figure 14.

5.3 Results based on varying the mass of TNT

The effect of varying the TNT mass on the geometry can produce significantly different structural response results. Different TNT masses provide differences in the explosive energy produced by the explosion on the geometry and can influence the stress received by the material and the force absorbed during the explosion. This CONWEP simulation used variations in the explosion load given to the geometry

Table 7: MADM criteria parameter values

Mass of TNT	Geometry	Thickness	Material	Annotation	Deflection C1	von mises stress C2	Energy dissipation C3
m5	G1	t1	Domex 700 steel	I	1.34×10^{-02}	1.17×10^{03}	7.05×10^{00}
m5	G1	t2	Domex 700 steel	II	9.06×10^{-03}	9.39×10^{02}	2.93×10^{00}
m5	G1	t3	Domex 700 steel	III	6.60×10^{-03}	9.18×10^{02}	2.64×10^{00}
m5	G1	t4	Domex 700 steel	IV	5.16×10^{-03}	9.11×10^{02}	1.72×10^{00}
m5	G1	t5	Domex 700 steel	V	4.14×10^{-03}	8.88×10^{02}	1.22×10^{00}
m5	G1	t1	1100 steel	VI	1.35×10^{-02}	1.18×10^{03}	1.92×10^{01}
m5	G1	t2	1100 steel	VII	9.22×10^{-03}	1.18×10^{03}	1.90×10^{01}
m5	G1	t3	1100 steel	VIII	8.54×10^{-03}	1.17×10^{03}	1.69×10^{01}
m5	G1	t4	1100 steel	IX	6.83×10^{-03}	1.16×10^{03}	1.15×10^{01}
m5	G1	t5	1100 steel	X	5.69×10^{-03}	1.14×10^{03}	7.05×10^{00}
m1	G1	t2	Domex 700 steel	XI	3.55×10^{-03}	8.67×10^{02}	4.96×10^{-01}
m2	G1	t2	Domex 700 steel	XII	4.98×10^{-03}	8.74×10^{02}	8.40×10^{-01}
m4	G1	t2	Domex 700 steel	XIII	6.34×10^{-03}	8.86×10^{02}	1.18×10^{00}
m5	G1	t2	Domex 700 steel	XIV	7.65×10^{-03}	8.97×10^{02}	1.66×10^{00}
m6	G1	t2	Domex 700 steel	XV	9.06×10^{-03}	9.14×10^{02}	3.03×10^{00}
m7	G1	t2	Domex 700 steel	XVI	1.02×10^{-02}	9.19×10^{02}	3.52×10^{00}
m1	G1	t2	1100 steel	XVII	3.57×10^{-03}	1.12×10^{03}	4.86×10^{00}
m2	G1	t2	1100 steel	XVIII	5.00×10^{-03}	1.13×10^{03}	6.72×10^{00}
m4	G1	t2	1100 steel	XIX	6.38×10^{-03}	1.15×10^{03}	1.00×10^{01}
m5	G1	t2	1100 steel	XX	7.68×10^{-03}	1.16×10^{03}	1.04×10^{01}
m6	G1	t2	1100 steel	XXI	1.02×10^{-02}	1.16×10^{03}	1.28×10^{01}
m7	G1	t2	1100 steel	XXII	1.14×10^{-02}	1.16×10^{03}	1.41×10^{01}
m1	G2	t2	Domex 700 steel	XXIII	3.43×10^{-03}	9.22×10^{02}	3.39×10^{00}
m2	G2	t2	Domex 700 steel	XXIV	4.81×10^{-03}	9.28×10^{02}	3.95×10^{00}
m3	G2	t2	Domex 700 steel	XXV	6.11×10^{-03}	9.33×10^{02}	7.22×10^{00}
m4	G2	t2	Domex 700 steel	XXVI	7.37×10^{-03}	9.58×10^{02}	7.79×10^{00}
m5	G2	t2	Domex 700 steel	XXVII	8.62×10^{-03}	9.65×10^{02}	8.09×10^{00}
m6	G2	t2	Domex 700 steel	XXVIII	9.83×10^{-03}	9.65×10^{02}	1.11×10^{01}
m7	G2	t2	Domex 700 steel	XXIX	1.18×10^{-02}	9.72×10^{02}	1.16×10^{01}
m1	G2	t2	1100 steel	XXX	3.57×10^{-03}	1.19×10^{03}	1.74×10^{01}
m2	G2	t2	1100 steel	XXXI	5.01×10^{-03}	1.20×10^{03}	1.85×10^{01}
m3	G2	t2	1100 steel	XXXII	6.26×10^{-03}	1.21×10^{03}	1.93×10^{01}
m4	G2	t2	1100 steel	XXXIII	7.47×10^{-03}	1.21×10^{03}	2.34×10^{01}
m5	G2	t2	1100 steel	XXXIV	8.89×10^{-03}	1.22×10^{03}	3.45×10^{01}
m6	G2	t2	1100 steel	XXXV	1.01×10^{-02}	1.23×10^{03}	3.94×10^{01}
m7	G2	t2	1100 steel	XXXVI	1.12×10^{-02}	1.26×10^{03}	6.35×10^{01}
m1	G3	t2	Domex 700 steel	XXXVII	3.31×10^{-03}	9.37×10^{02}	4.33×10^{00}
m2	G3	t2	Domex 700 steel	XXXVIII	4.67×10^{-03}	9.47×10^{02}	7.33×10^{00}
m3	G3	t2	Domex 700 steel	XXXIX	5.92×10^{-03}	9.56×10^{02}	9.51×10^{00}
m4	G3	t2	Domex 700 steel	XL	7.15×10^{-03}	9.64×10^{02}	1.27×10^{01}
m5	G3	t2	Domex 700 steel	XLI	8.32×10^{-03}	9.71×10^{02}	1.83×10^{01}
m6	G3	t2	Domex 700 steel	XLII	9.47×10^{-03}	9.80×10^{02}	2.42×10^{01}
m7	G3	t2	Domex 700 steel	XLIII	1.06×10^{-02}	9.93×10^{02}	6.23×10^{01}
m1	G3	t2	1100 steel	XLIV	3.60×10^{-03}	1.20×10^{03}	3.36×10^{01}
m2	G3	t2	1100 steel	XLV	5.07×10^{-03}	1.20×10^{03}	3.64×10^{01}
m3	G3	t2	1100 steel	XLVI	6.27×10^{-03}	1.23×10^{03}	5.60×10^{01}
m4	G3	t2	1100 steel	XLVII	7.40×10^{-03}	1.24×10^{03}	7.03×10^{01}
m5	G3	t2	1100 steel	XLVIII	9.00×10^{-03}	1.25×10^{03}	7.95×10^{01}
m6	G3	t2	1100 steel	XLIX	1.02×10^{-02}	1.25×10^{03}	8.31×10^{01}
m7	G3	t2	1100 steel	L	1.13×10^{-02}	1.25×10^{03}	8.43×10^{01}
m1	G4	t2	Domex 700 steel	LI	3.54×10^{-03}	8.13×10^{02}	1.20×10^{00}
m2	G4	t2	Domex 700 steel	LII	4.97×10^{-03}	8.91×10^{02}	2.02×10^{00}
m3	G4	t2	Domex 700 steel	LIII	6.32×10^{-03}	9.07×10^{02}	2.67×10^{00}
m4	G4	t2	Domex 700 steel	LIV	7.62×10^{-03}	9.19×10^{02}	3.92×10^{00}
m5	G4	t2	Domex 700 steel	LV	8.84×10^{-03}	9.28×10^{02}	5.20×10^{00}

(Continued)

Table 7: *Continued*

Mass of TNT	Geometry	Thickness	Material	Annotation	Deflection C1	von mises stress C2	Energy dissipation C3
m6	G4	t2	Domex 700 steel	LVI	9.26×10^{-03}	9.33×10^{02}	5.51×10^{00}
m7	G4	t2	Domex 700 steel	LVII	9.62×10^{-03}	9.80×10^{02}	6.05×10^{00}
m1	G5	t2	Domex 700 steel	LVIII	3.52×10^{-03}	9.16×10^{02}	4.07×10^{00}
m2	G5	t2	Domex 700 steel	LIX	4.92×10^{-03}	9.29×10^{02}	6.06×10^{00}
m3	G5	t2	Domex 700 steel	LX	6.27×10^{-03}	9.42×10^{02}	6.08×10^{00}
m4	G5	t2	Domex 700 steel	LXI	7.58×10^{-03}	9.45×10^{02}	6.93×10^{00}
m5	G5	t2	Domex 700 steel	LXII	8.83×10^{-03}	9.51×10^{02}	8.13×10^{00}
m6	G5	t2	Domex 700 steel	LXIII	9.69×10^{-03}	9.54×10^{02}	1.04×10^{01}
m7	G5	t2	Domex 700 steel	LXIV	1.01×10^{-02}	9.60×10^{02}	1.45×10^{01}
m1	G5	t2	1100 steel	LXV	3.51×10^{-03}	1.17×10^{03}	1.73×10^{01}
m2	G5	t2	1100 steel	LXVI	4.93×10^{-03}	1.19×10^{03}	2.61×10^{01}
m3	G5	t2	1100 steel	LXVII	6.29×10^{-03}	1.19×10^{03}	2.92×10^{01}
m4	G5	t2	1100 steel	LXVIII	7.61×10^{-03}	1.22×10^{03}	4.56×10^{01}
m5	G5	t2	1100 steel	LXIX	8.88×10^{-03}	1.22×10^{03}	5.50×10^{01}
m6	G5	t2	1100 steel	LXX	1.01×10^{-02}	1.22×10^{03}	5.53×10^{01}
m7	G5	t2	1100 steel	LXXI	1.13×10^{-02}	1.23×10^{03}	5.85×10^{01}

with two cross-stiffeners using the 1100 (D1100) steel material. The explosion load ranged from 10 to 40 g of TNT to determine the structural response exhibited by the geometry. The explosion results for variations in the TNT mass are shown in Figure 15.

Based on the deflection values obtained for the geometries with varying explosion masses, it was revealed that the explosion mass has a crucial role in the impact on the geometry. It was observed that an explosion mass of 10 g produced a deflection of 3.51 mm, which was the smallest deflection compared to an explosion mass of 40 g, which produced a deflection of 11.34 mm and was the most significant deflection obtained for the geometry due to the explosion. This shows that the mass of TNT has a crucial role in providing significant deflection changes to the geometry's ability to receive force and then absorb the force to produce a deflection.

The structural response of the geometry to the received von Mises stress and the energy dissipation were 1,421 Pa and 629.8 J. The analysis results showed that a TNT mass of 10 g obtained after the explosion indicated that the energy dissipation capability and the von Mises stress peaked at these values. However, a TNT mass of 15–40 g showed a different structural response because these values were obtained when the explosion was not complete relative to the geometry. The illustration of the von Mises stress and the energy dissipation contours shown in Figures 15 and 16 can explain that a higher explosion mass caused a higher von Mises stress value, thus affecting the geometry's ability to absorb energy and influencing the deflection that occurred.

5.4 Results based on variations in geometry

Variations in the geometry significantly impacted the blast's structural response. In the numerical simulations with variations in the geometry, a stiffener on a circular plate was used to analyze the influence received. These used aspects of deflection, von Mises stress, and energy dissipation. The number, position, and spacing of the stiffener can substantially affect the structural response to blast loading. Figure 17 shows the deflection results obtained for each geometric variation.

Numerical simulations using the CONWEP method were carried out on the geometry using Domex 1100 (D1100) steel material with an explosion load of 30 g. The results of the deflection data showed that the largest deflection was obtained with an unstiffened circular plate, at 9.37 mm, and the smallest deflection was obtained for a circular plate with one cross-stiffener, with a deflection value of 9 mm. Through the deflection value obtained due to the explosion, the von Mises stress value and the energy absorbed by the geometry played a role in the deflection of the geometry. It can be explained that the structural response to geometric variations significantly influenced the explosion, as illustrated in Figure 18.

The results of the numerical simulation data analysis showed that variations in the geometry with stiffeners on circular plates resulted in quite impressive differences in the structural response in terms of the von Mises stress and the energy dissipation at values of 1,120 Pa and 289 J. This shows that the number and distance of stiffeners in

Table 8: MADM data normalization

Mass of TNT	Geometry	Thickness	Material	Annotation	Deflection C1 0.00331	von Mises stress C2 813.455	Energy dissipation C3 0.4958
m5	G1	t1	Domex 700 steel	I	1.23×10^{-01}	2.31×10^{-01}	1.17×10^{-02}
m5	G1	t2	Domex 700 steel	II	4.51×10^{-02}	2.00×10^{-01}	1.99×10^{-03}
m5	G1	t3	Domex 700 steel	III	2.26×10^{-02}	1.77×10^{-01}	3.73×10^{-04}
m5	G1	t4	Domex 700 steel	IV	1.45×10^{-02}	1.58×10^{-01}	1.08×10^{-04}
m5	G1	t5	Domex 700 steel	V	1.16×10^{-02}	1.45×10^{-01}	4.37×10^{-05}
m5	G1	t1	1100 steel	VI	2.85×10^{-03}	9.95×10^{-02}	1.13×10^{-06}
m5	G1	t2	1100 steel	VII	1.02×10^{-03}	6.87×10^{-02}	2.94×10^{-08}
m5	G1	t3	1100 steel	VIII	3.97×10^{-04}	4.76×10^{-02}	8.61×10^{-10}
m5	G1	t4	1100 steel	IX	1.92×10^{-04}	3.35×10^{-02}	3.73×10^{-11}
m5	G1	t5	1100 steel	X	1.12×10^{-04}	2.39×10^{-02}	2.62×10^{-12}
m1	G1	t2	Domex 700 steel	XI	1.04×10^{-04}	2.24×10^{-02}	2.62×10^{-12}
m2	G1	t2	Domex 700 steel	XII	6.93×10^{-05}	2.09×10^{-02}	1.55×10^{-12}
m4	G1	t2	Domex 700 steel	XIII	3.62×10^{-05}	1.92×10^{-02}	6.53×10^{-13}
m5	G1	t2	Domex 700 steel	XIV	1.56×10^{-05}	1.74×10^{-02}	1.95×10^{-13}
m6	G1	t2	Domex 700 steel	XV	5.72×10^{-06}	1.55×10^{-02}	3.20×10^{-14}
m7	G1	t2	Domex 700 steel	XVI	1.86×10^{-06}	1.37×10^{-02}	4.50×10^{-15}
m1	G1	t2	1100 steel	XVII	1.73×10^{-06}	9.96×10^{-03}	4.60×10^{-16}
m2	G1	t2	1100 steel	XVIII	1.14×10^{-06}	7.18×10^{-03}	3.39×10^{-17}
m4	G1	t2	1100 steel	XIX	5.94×10^{-07}	5.08×10^{-03}	1.67×10^{-18}
m5	G1	t2	1100 steel	XX	2.56×10^{-07}	3.57×10^{-03}	7.99×10^{-20}
m6	G1	t2	1100 steel	XXI	8.30×10^{-08}	2.50×10^{-03}	3.09×10^{-21}
m7	G1	t2	1100 steel	XXII	2.41×10^{-08}	1.75×10^{-03}	1.08×10^{-22}
m1	G2	t2	Domex 700 steel	XXIII	2.32×10^{-08}	1.54×10^{-03}	1.58×10^{-23}
m2	G2	t2	Domex 700 steel	XXIV	1.60×10^{-08}	1.35×10^{-03}	1.99×10^{-24}
m3	G2	t2	Domex 700 steel	XXV	8.66×10^{-09}	1.18×10^{-03}	1.37×10^{-25}
m4	G2	t2	Domex 700 steel	XXVI	3.89×10^{-09}	1.00×10^{-03}	8.69×10^{-27}
m5	G2	t2	Domex 700 steel	XXVII	1.49×10^{-09}	8.44×10^{-04}	5.32×10^{-28}
m6	G2	t2	Domex 700 steel	XXVIII	5.03×10^{-10}	7.11×10^{-04}	2.38×10^{-29}
m7	G2	t2	Domex 700 steel	XXIX	1.41×10^{-10}	5.95×10^{-04}	1.02×10^{-30}
m1	G2	t2	1100 steel	XXX	1.31×10^{-10}	4.07×10^{-04}	2.91×10^{-32}
m2	G2	t2	1100 steel	XXXI	8.65×10^{-11}	2.76×10^{-04}	7.79×10^{-34}
m3	G2	t2	1100 steel	XXXII	4.58×10^{-11}	1.86×10^{-04}	2.00×10^{-35}
m4	G2	t2	1100 steel	XXXIII	2.03×10^{-11}	1.25×10^{-04}	4.24×10^{-37}
m5	G2	t2	1100 steel	XXXIV	7.55×10^{-12}	8.33×10^{-05}	6.08×10^{-39}
m6	G2	t2	1100 steel	XXXV	2.48×10^{-12}	5.49×10^{-05}	7.66×10^{-41}
m7	G2	t2	1100 steel	XXXVI	7.35×10^{-13}	3.54×10^{-05}	5.98×10^{-43}
m1	G3	t2	Domex 700 steel	XXXVII	7.35×10^{-13}	3.07×10^{-05}	6.85×10^{-44}
m2	G3	t2	Domex 700 steel	XXXVIII	5.21×10^{-13}	2.64×10^{-05}	4.63×10^{-45}
m3	G3	t2	Domex 700 steel	XXXIX	2.91×10^{-13}	2.25×10^{-05}	2.42×10^{-46}
m4	G3	t2	Domex 700 steel	XL	1.35×10^{-13}	1.90×10^{-05}	9.42×10^{-48}
m5	G3	t2	Domex 700 steel	XLI	5.37×10^{-14}	1.59×10^{-05}	2.56×10^{-49}
m6	G3	t2	Domex 700 steel	XLII	1.88×10^{-14}	1.32×10^{-05}	5.24×10^{-51}
m7	G3	t2	Domex 700 steel	XLIII	5.84×10^{-15}	1.08×10^{-05}	4.17×10^{-53}
m1	G3	t2	1100 steel	XLIV	5.37×10^{-15}	7.32×10^{-06}	6.16×10^{-55}
m2	G3	t2	1100 steel	XLV	3.51×10^{-15}	4.95×10^{-06}	8.40×10^{-57}
m3	G3	t2	1100 steel	XLVI	1.85×10^{-15}	3.27×10^{-06}	7.44×10^{-59}
m4	G3	t2	1100 steel	XLVII	8.28×10^{-16}	2.14×10^{-06}	5.24×10^{-61}
m5	G3	t2	1100 steel	XLVIII	3.05×10^{-16}	1.39×10^{-06}	3.27×10^{-63}
m6	G3	t2	1100 steel	XLIX	9.91×10^{-17}	9.07×10^{-07}	1.95×10^{-65}
m7	G3	t2	1100 steel	L	2.90×10^{-17}	5.89×10^{-07}	1.15×10^{-67}
m1	G4	t2	Domex 700 steel	LI	2.71×10^{-17}	5.89×10^{-07}	4.72×10^{-68}
m2	G4	t2	Domex 700 steel	LII	1.81×10^{-17}	5.38×10^{-07}	1.16×10^{-68}
m3	G4	t2	Domex 700 steel	LIII	9.46×10^{-18}	4.82×10^{-07}	2.15×10^{-69}
m4	G4	t2	Domex 700 steel	LIV	4.11×10^{-18}	4.27×10^{-07}	2.72×10^{-70}

(Continued)

Table 8: *Continued*

Mass of TNT	Geometry	Thickness	Material	Annotation	Deflection C1 0.00331	von Mises stress C2 813.455	Energy dissipation C3 0.4958
m5	G4	t2	Domex 700 steel	LV	1.54×10^{-18}	3.74×10^{-07}	2.60×10^{-71}
m6	G4	t2	Domex 700 steel	LVI	5.50×10^{-19}	3.26×10^{-07}	2.34×10^{-72}
m7	G4	t2	Domex 700 steel	LVII	1.89×10^{-19}	2.71×10^{-07}	1.91×10^{-73}
m1	G5	t2	Domex 700 steel	LVIII	1.78×10^{-19}	2.41×10^{-07}	2.33×10^{-74}
m2	G5	t2	Domex 700 steel	LIX	1.20×10^{-19}	2.11×10^{-07}	1.91×10^{-75}
m3	G5	t2	Domex 700 steel	LX	6.32×10^{-20}	1.82×10^{-07}	1.56×10^{-76}
m4	G5	t2	Domex 700 steel	LXI	2.76×10^{-20}	1.57×10^{-07}	1.11×10^{-77}
m5	G5	t2	Domex 700 steel	LXII	1.03×10^{-20}	1.34×10^{-07}	6.79×10^{-79}
m6	G5	t2	Domex 700 steel	LXIII	3.53×10^{-21}	1.14×10^{-07}	3.24×10^{-80}
m7	G5	t2	Domex 700 steel	LXIV	1.15×10^{-21}	9.68×10^{-08}	1.11×10^{-81}
m1	G5	t2	1100 steel	LXV	1.09×10^{-21}	6.73×10^{-08}	3.17×10^{-83}
m2	G5	t2	1100 steel	LXVI	7.31×10^{-22}	4.61×10^{-08}	6.01×10^{-85}
m3	G5	t2	1100 steel	LXVII	3.85×10^{-22}	3.14×10^{-08}	1.02×10^{-86}
m4	G5	t2	1100 steel	LXVIII	1.67×10^{-22}	2.10×10^{-08}	1.11×10^{-88}
m5	G5	t2	1100 steel	LXIX	6.24×10^{-23}	1.40×10^{-08}	9.99×10^{-91}
m6	G5	t2	1100 steel	LXX	2.04×10^{-23}	9.33×10^{-09}	8.96×10^{-93}
m7	G5	t2	1100 steel	LXXI	5.95×10^{-24}	6.18×10^{-09}	7.60×10^{-95}

the geometry affected the performance. The geometry defines the ability of the structure to absorb energy when receiving stress from outside. The areas that receive the highest stress, on average, are at the end of the stiffeners and the edge of the geometry due to being connected to the clamp and experiencing energy absorption, resulting in plastic deformation.

5.5 MADM analysis

MADM is an approach that is used to make decisions and evaluate several alternatives based on relevant criteria. The impact of the circular plate on blast loading was analyzed to validate the results of the numerical simulations using the CONWEP method. There is an initial stage in carrying out MADM, namely determining the score from the parameters used and proceeding to the next stage by entering the test result data according to the parameters that have been determined. The parameters used in analyzing MADM were the deflection, von Mises stress, and energy dissipation by taking the value of each criterion when it reached 0.5 ms. The value data for each criterion from the numerical simulation results are shown in Table 7.

In the next stage, the inputted data were subjected to a data normalization process for further analysis to avoid data anomalies. For each criterion, which consisted of C1 (deflection), C2 (von Mises stress), and C3 (energy dissipation), the smallest data value was taken. This was chosen because the smaller the deflection value, the smaller the value of the von Mises stress and the energy dissipation, as the force received and the energy absorbed did not cause the deflection to become more significant. Therefore, the structural response that occurred was considered better. The data normalization results for each numerical simulation data result are presented in Table 8.

After the data were normalized, the next stage was to carry out assessment calculations on MADM, assuming that the numerical simulation results with the highest score are considered the best results. Then, after each data result had been given a score, ranking was carried out to determine the numerical simulation results with the most significant score values. The calculation results and data ranking of the numerical simulation results are shown in Table 9.

The ranked results were divided into fifths, and each fifth consisted of 14 numerical simulations, from the smallest to the largest. The larger value of the total weight gained in each fifth indicated that the results obtained were worse. Based on the above data, the best-ranked results were in the first fifth, with annotations from LXXI to LVIII and the lowest score of 6.176×10^{-09}. The worst-ranked result was in the last fifth, with annotations from XV to I and a top score of 3.659×10^{-01}.

Table 9: Overall results and MADM ranking

Mass of TNT	Geometry	Thickness	Material	Annotation	Total weight	Ranking
m7	G5	t2	1100 steel	LXXI	6.176×10^{-09}	1
m6	G5	t2	1100 steel	LXX	9.330×10^{-09}	2
m5	G5	t2	1100 steel	LXIX	1.400×10^{-08}	3
m4	G5	t2	1100 steel	LXVIII	2.098×10^{-08}	4
m3	G5	t2	1100 steel	LXVII	3.140×10^{-08}	5
m2	G5	t2	1100 steel	LXVI	4.607×10^{-08}	6
m1	G5	t2	1100 steel	LXV	6.726×10^{-08}	7
m7	G5	t2	Domex 700 steel	LXIV	9.677×10^{-08}	8
m6	G5	t2	Domex 700 steel	LXIII	1.143×10^{-07}	9
m5	G5	t2	Domex 700 steel	LXII	1.340×10^{-07}	10
m4	G5	t2	Domex 700 steel	LXI	1.567×10^{-07}	11
m3	G5	t2	Domex 700 steel	LX	1.821×10^{-07}	12
m2	G5	t2	Domex 700 steel	LIX	2.109×10^{-07}	13
m1	G5	t2	Domex 700 steel	LVIII	2.407×10^{-07}	14
m7	G4	t2	Domex 700 steel	LVII	2.711×10^{-07}	15
m6	G4	t2	Domex 700 steel	LVI	3.265×10^{-07}	16
m5	G4	t2	Domex 700 steel	LV	3.744×10^{-07}	17
m4	G4	t2	Domex 700 steel	LIV	4.271×10^{-07}	18
m3	G4	t2	Domex 700 steel	LIII	4.823×10^{-07}	19
m2	G4	t2	Domex 700 steel	LII	5.377×10^{-07}	20
m1	G4	t2	Domex 700 steel	LI	5.887×10^{-07}	21
m7	G3	t2	1100 steel	L	5.887×10^{-07}	22
m6	G3	t2	1100 steel	XLIX	9.075×10^{-07}	23
m5	G3	t2	1100 steel	XLVIII	1.394×10^{-06}	24
m4	G3	t2	1100 steel	XLVII	2.139×10^{-06}	25
m3	G3	t2	1100 steel	XLVI	3.267×10^{-06}	26
m2	G3	t2	1100 steel	XLV	4.949×10^{-06}	27
m1	G3	t2	1100 steel	XLIV	7.323×10^{-06}	28
m7	G3	t2	Domex 700 steel	XLIII	1.082×10^{-05}	29
m6	G3	t2	Domex 700 steel	XLII	1.320×10^{-05}	30
m5	G3	t2	Domex 700 steel	XLI	1.590×10^{-05}	31
m4	G3	t2	Domex 700 steel	XL	1.898×10^{-05}	32
m3	G3	t2	Domex 700 steel	XXXIX	2.248×10^{-05}	33
m2	G3	t2	Domex 700 steel	XXXVIII	2.642×10^{-05}	34
m1	G3	t2	Domex 700 steel	XXXVII	3.075×10^{-05}	35
m7	G2	t2	1100 steel	XXXVI	3.541×10^{-05}	36
m6	G2	t2	1100 steel	XXXV	5.488×10^{-05}	37
m5	G2	t2	1100 steel	XXXIV	8.327×10^{-05}	38
m4	G2	t2	1100 steel	XXXIII	1.245×10^{-04}	39
m3	G2	t2	1100 steel	XXXII	1.857×10^{-04}	40
m2	G2	t2	1100 steel	XXXI	2.761×10^{-04}	41
m1	G2	t2	1100 steel	XXX	4.067×10^{-04}	42
m7	G2	t2	Domex 700 steel	XXIX	5.951×10^{-04}	43
m6	G2	t2	Domex 700 steel	XXVIII	7.111×10^{-04}	44
m5	G2	t2	Domex 700 steel	XXVII	8.439×10^{-04}	45
m4	G2	t2	Domex 700 steel	XXVI	1.001×10^{-03}	46
m3	G2	t2	Domex 700 steel	XXV	1.179×10^{-03}	47
m2	G2	t2	Domex 700 steel	XXIV	1.352×10^{-03}	48
m1	G2	t2	Domex 700 steel	XXIII	1.543×10^{-03}	49
m7	G1	t2	1100 steel	XXII	1.749×10^{-03}	50
m6	G1	t2	1100 steel	XXI	2.504×10^{-03}	51
m5	G1	t2	1100 steel	XX	3.573×10^{-03}	52
m4	G1	t2	1100 steel	XIX	5.077×10^{-03}	53
m2	G1	t2	1100 steel	XVIII	7.182×10^{-03}	54
m1	G1	t2	1100 steel	XVII	9.962×10^{-03}	55
m7	G1	t2	Domex 700 steel	XVI	1.370×10^{-02}	56

(Continued)

Table 9: *Continued*

Mass of TNT	Geometry	Thickness	Material	Annotation	Total weight	Ranking
m6	G1	t2	Domex 700 steel	XV	1.549×10^{-02}	57
m5	G1	t2	Domex 700 steel	XIV	1.741×10^{-02}	58
m4	G1	t2	Domex 700 steel	XIII	1.920×10^{-02}	59
m2	G1	t2	Domex 700 steel	XII	2.094×10^{-02}	60
m1	G1	t2	Domex 700 steel	XI	2.254×10^{-02}	61
m5	G1	t5	1100 steel	X	2.403×10^{-02}	62
m5	G1	t4	1100 steel	IX	3.366×10^{-02}	63
m5	G1	t3	1100 steel	VIII	4.798×10^{-02}	64
m5	G1	t2	1100 steel	VII	6.975×10^{-02}	65
m5	G1	t1	1100 steel	VI	1.024×10^{-01}	66
m5	G1	t5	Domex 700 steel	V	1.565×10^{-01}	67
m5	G1	t4	Domex 700 steel	IV	1.728×10^{-01}	68
m5	G1	t3	Domex 700 steel	III	2.001×10^{-01}	69
m5	G1	t2	Domex 700 steel	II	2.469×10^{-01}	70
m5	G1	t1	Domex 700 steel	I	3.659×10^{-01}	71

5.6 Sensitivity analysis

The sensitivity analysis in this research used the regression method to obtain the coefficient values, standard error, *R*-squared value, *P*-value, and significant *F*-value, which helped to analyze the impact of the variations in the material, the mass of TNT, the thickness, and the geometry on the explosions. In applying the sensitivity analysis, the carbon content, mass of TNT, stiffener volume, and thickness became the input variables for the variations in the numerical simulation, which resulted in the deflection, von Mises stress, and energy dissipation. A high *R*-squared value indicates that a variable significantly influences the geometric structural response. The coefficient value describes how much a change in the independent variable contributes to the average change in the dependent variable. The greater the coefficient value, the more significant the influence of variation on the numerical results.

The standard error value shows how far the average value is from the regression line and how accurate the

Table 10: Sensitivity analysis of criteria

	Variable			
Indicator	**Thickness**	**Mass of TNT**	**%C**	**Stiffener volume**
		Deflection		
Coefficient	-1.14×10^{-03}	1.22×10^{-03}	1.10×10^{-02}	-1.91×10^{-07}
Standard error	2.53×10^{-03}	2.53×10^{-03}	2.63×10^{-03}	2.63×10^{-03}
P-values	1.83×10^{-02}	7.33×10^{-25}	4.86×10^{-01}	7.54×10^{-01}
R-squared value	7.81×10^{-02}	7.87×10^{-01}	7.06×10^{-03}	1.43×10^{-03}
Significant *F*-value	1.83×10^{-02}	7.33×10^{-25}	4.86×10^{-01}	7.54×10^{-01}
		Stress		
Coefficient	-2.08×10^{01}	2.12×10^{00}	6.50×10^{03}	1.40×10^{-02}
Standard error	1.39×10^{02}	1.38×10^{02}	4.69×10^{01}	1.39×10^{02}
P-values	4.25×10^{-01}	2.19×10^{-01}	2.41×10^{-34}	6.63×10^{-01}
R-squared value	9.23×10^{-03}	2.18×10^{-02}	8.87×10^{-01}	2.76×10^{-03}
Significant *F*-value	4.25×10^{-01}	2.19×10^{-01}	2.41×10^{-34}	6.63×10^{-01}
		Energy dissipation		
Coefficient	-5.24×10^{00}	7.49×10^{-01}	6.50×10^{02}	1.30×10^{-02}
Standard error	2.19×10^{01}	2.10×10^{01}	1.79×10^{01}	2.11×10^{01}
P-values	2.06×10^{-01}	5.38×10^{-03}	5.63×10^{-08}	9.19×10^{-03}
R-squared value	2.31×10^{-02}	1.07×10^{-01}	3.50×10^{-01}	9.43×10^{-02}
Significant *F*-value	2.06×10^{-01}	5.38×10^{-03}	5.63×10^{-08}	9.19×10^{-03}

regression line is at predicting the response variable. The significant *F*-value in the regression analysis shows the extent to which the regression model fits the observed data compared to models that do not use predictor variables. The lower the significant *F*-value, the greater the impact of the variations on the final results produced by the regression model. The results of the sensitivity analysis of the criteria are shown in Table 10.

Based on the data above, the deflection criterion showed that the mass of TNT had a significant effect, as it obtained the highest *R*-squared value and the smallest significant *F*-value. In addition, the larger coefficient, standard error, and *P*-values indicated that the mass of TNT had little influence on the final results. The sensitivity analysis results on the von Mises stress criterion showed that the carbon content had a significant influence due to having the highest *R*-squared value and the smallest significant *F*-value. In addition, the smaller coefficient, standard error, and *P*-values for the von Mises stress criterion indicated that the carbon content significantly influenced the final result. The energy dissipation criterion showed that the carbon content had a significant effect because it had the largest *R*-squared value and the smallest significant *F*-value. In addition, a larger coefficient value indicated that the carbon content had little influence on the results. Meanwhile, the *P*-value and standard error, which became smaller, indicated that the different carbon content had an influence and an impact on the final results. Thus, changes in the mass of TNT significantly impacted the deflection. Meanwhile, the carbon content had an impact on the stress and energy dissipation in the geometry.

6 Conclusions

This research aimed to comprehensively analyze and evaluate the structural response performance of circular plates with geometric variations combined with various parameters against explosions.

1. Each numerical simulation with various combinations yielded results that significantly affected the geometry. In addition, the numerical simulation results were validated using the MADM method and a sensitivity analysis.
2. In the MADM process, the best simulation results were obtained with annotations from LXXI to LVIII and the lowest score of 6.176×10^{-09}. The results with the worst ranking were in the fifth to last position, with annotations from XV to I and the highest score of 3.659×10^{-01}. The geometry of the circular plate and two cross-stiffeners in this variation obtained the smallest and largest von Mises stress, deflection, and energy dissipation from a total of 71 numerical simulation data results, thereby demonstrating the structural response performance of the circular plate to an explosion.
3. The sensitivity analysis explained that the mass of TNT and the carbon content in the material significantly influenced the numerical simulation results in producing von Mises stress, deflection, and energy dissipation. This explains that the stress and energy dissipation values influence the amount of deflection. The mass of TNT and the carbon content can also affect these three values.

Acknowledgments: This work is part of a collaboration project between the Faculty of Engineering, Universitas Sebelas Maret (UNS), and Research Center of Testing Technology and Standard, National Research and Innovation Agency (BRIN) with Collaboration Agreement Numbers 179/V/KS/06/2024 and 541/UN27.08.1/HK.07.00/2024.

Funding information: Authors state no funding involved.

Author contributions: All authors have accepted responsibility for the entire content of this manuscript and consented to its submission to the journal, reviewed all the results, and approved the final version of the manuscript. AFFKA: writing – original draft, validation, formal analysis, data curation, investigation. TM: supervision, conceptualization, methodology. ARP: methodology, project administration, supervision, writing – review and editing, project administration, funding acquisition. BD: investigation, writing – review and editing. QTD: visualization, writing – review and editing. HS: supervision, methodology, conceptualization. SJB: data curation, investigation. BDT: visualization, conceptualization.

Conflict of interest: Authors state no conflict of interest.

Data availability statement: The authors confirm that the data supporting the findings of this study are available within the article.

References

[1] Transportation Safety Board of Canada, Marine Transportation Occurrences in 2021 https://www.tsb.gc.ca/eng/stats/marine/2021/ssem-ssmo-2021.html (accessed April. 5, 2024).

[2] Mujeed-Ahmed MP, Ince ST, Paik JK. Computational models for the structural crashworthiness analysis of a fixed-type offshore platform in collisions with an offshore supply vessel. Thin Wall Struct. 2020;154:106868. doi: 10.1016/j.tws.2020.106868.

[3] Zhe-Nian X, Min-Xie Q, Li-Kong X, Kang-Yao Y, Huang K. Experimental and numerical study on protective effect of RC blast wall against air shock wave. Def Technol. 2024;31:567–79. doi: 10.1016/j.dt.2022.11.005.
[4] Tian S, Yan Q, Du X, Chen F, Zhang B. Experimental and numerical studies on the dynamic response of precast concrete slabs under blast load. J Build Eng. 2023;70:106425. doi: 10.1016/j.jobe.2023.106425.
[5] Barsoum I, Lawal SA, Simmons RJ, Rodrigues CC. Failure analysis of a pressure vessel subjected to an internal blast load. Eng Fail Anal. 2018;91:354–69. doi: 10.1016/j.engfailanal.2018.04.037.
[6] Mohamed MN. Improving the blast resistance of sandwich structures by tailoring honeycomb core through varying cell size and vertex-derivative approach. Forc Mech. 2023;13:100247. doi: 10.1016/j.finmec.2023.100247.
[7] Schunck T, Eckenfels D, Sinniger L. Blast disruption using 3D grids/perforated plates for vehicle protection. Def Technol. 2023;25:60–8. doi: 10.1016/j.dt.2022.10.005.
[8] Mubarok MAH, Prabowo AR, Muttaqie T, Muhayat N. Dynamic structural assessment of blast wall designs on military-based vehicle using explicit finite element approach. Math Probl Eng. 2022;2022:5883404. doi: 10.1155/2022/5883404.
[9] Zakrisson B, Wikman B, Häggblad H. Numerical simulations of blast loads and structural deformation from near-field explosions in air. Int J Impact Eng. 2011;8(11):597–612. doi: 10.1016/j.ijimpeng.2011.02.005.
[10] Patel M, Patel S. Effect of honeycomb cell size on the air-blast performance of sandwich panels. Mat Today Proc. 2023;78(4):792–7. doi: 10.1016/j.matpr.2022.10.283.
[11] Saifi F, Anas SM, Tahzeeb R, Shariq M, Alam M. Numerical investigation of blast loading effects on a thin-walled cylindrical steel storage tank. Mat Today Proc. 2024. doi: 10.1016/j.matpr.2024.04.001.
[12] Maulana MI, Prabowo AR, Muttaqie E, Muhayat N, Tjahjana DD, Do QT, et al. Analysis of the idealized steel pipe under internal explosive loading: Comparison between FE approach and laboratory experiment. Proc Struct Integr. 2023;47:150–8. doi: 10.1016/j.prostr.2023.07.006.
[13] Mubarok MAH, Muttaqie T, Prabowo AR, Sohn JM, Surojo E, Imaduddin F. Effects of geometrical variations on the performance of hull plate structures under blast load: a study using nonlinear FEA. Proc Struct Integr. 2022;41:282–9. doi: 10.1016/j.prostr.2022.05.033.
[14] Satouri S, Kargarnovin MH, Allahkarami F, Asanjarani A. Application of third order shear deformation theory in buckling analysis of 2D functionally graded cylindrical shell reinforced by axial stiffeners. Compos Part B. 2015;79:236–53. doi: 10.1016/j.compositesb.2015.04.036.
[15] Ajeesh SS, Jayachandran AA. Computation of shear buckling stress of thin walled sections using constrained spline finite strip method. Thin Wall Struct. 2024;199:111813. doi: 10.1016/j.tws.2024.111813.
[16] Sedmak A, Grbović A, Zaidi R, Kirin S, Vitas N, Golubović T, et al. Numerical, analytical and experimental determination of remaining life of a pipe with an axial crack. Struct Integr Life. 2023;23(3):239–44.
[17] Dinulović M, Grbović A, Adžić V, Alarafati H. Composite plates with nomex honeycomb core modelling for dynamic integrity at the mesoscale level. Struct Integr. Life. 2023;23(2):147–53.
[18] Achira FSK, Medjdoub SM, Hocine A, Dhaou MH, Chapelle D. Numerical analysis of the effect of the repair of corroded pipe. Struct Integr Life. 2023;23(1):15–22.
[19] Lazerević M, Živković B, Bajić D, Alil A, Tomić L, Nedić B. Properties of aluminium-steel plates explosively welded using amonex. Struct Integr Life. 2023;23(2):141–6.
[20] Lee J, Lacy Jr TE, Pittman Jr CU. Lightning mechanical damage prediction in carbon/epoxy laminates using equivalent air blast overpressure. Compos Part B Eng. 2021;212:108649. doi: 10.1016/j.compositesb.2021.108649.
[21] Qi SB, Huang GY, Zhi XD, Fan F. Sensitivity analysis and probability modelling of the structural response of a single-layer reticulated dome subjected to an external blast loading. Def Technol. 2023;23:152–63. doi: 10.1016/j.dt.2022.02.004.
[22] Wang LJ, Wang T, Cheng S, Yin WJ, Liao Z. Difference analysis of different explosion load simulation methods based on LS-DYNA. J Phys Conf. 2022;2478:072053. doi: 10.1088/1742-6596/2478/7/072053.
[23] Aouad CJ, Chemissany W, Mazzali P, Temsah Y, Jahami A. Beirut explosions: TNT equivalence from the fireball evolution in the first 170 miliseconds. Shock Wave. 2021;31:813–27. doi: 10.1007/s00193-021-01031-9.
[24] Povey MJW. Scattering of sound. Ultrasonic techniques for fluid characterization. Massachusetts: Academic Press; 1997.
[25] Peyman S, Eskandari A. Analytical and numerical study of concrete slabs reinforced by steel rebars and perforated steel plates under blast loading. Mat Today Proc. 2023;19:101319. doi: 10.1016/j.rineng.2023.101319.
[26] Zhang T, Liu Z, Li S, Lei J, Wang Z. Dynamic response and energy absorption performance of aluminum foam-filled sandwich circular tubes under internal blast loading. Int J Impact Eng. 2023;173:104458. doi: 10.1016/j.ijimpeng.2022.104458.
[27] Lin L, Huo M. Effectiveness of composite energy dissipation restrainer on mitigating pounding and unseating failure of highway bridges. Struct. 2024;63:106361. doi: 10.1016/j.istruc.2024.106361.
[28] Ansori DT, Prabowo AR, Muttaqie T, Muhayat N, Laksono FB, Tjahjana DD, et al. Investigation of honeycomb sandwich panel structure using aluminum alloy (AL6XN) material under blast loading. Civ Eng J. 2022;8:1046–68. doi: 10.28991/CEJ-2022-08-05-014.
[29] Si D, Pan Z, Zhang H. Determination method of mesh size for numerical simulation of blast load in near-ground detonation. Def Technol. 2024;38:111–25. doi: 10.1016/j.dt.2023.08.004.
[30] Henchie TF, Yuen SC, Nurick GN, Ranwaha N, Balden VH. The response of circular plates to repeated uniform blast loads: An experimental and numerical study. Int J Impact Eng. 2014;74:36–45. doi: 10.1016/j.ijimpeng.2014.02.021.
[31] Pratomo AN, Santosa SP, Gunawan L, Putra IS, Dirgantara T, Widagdo D. Numerical study of experiment setup for aluminum foam sandwich construction subjected to blast load. Mesin. 2018;27:19–31. doi: 10.5614/MESIN.2018.27.1.3.
[32] González R, García JO, Barbés MA, Quintana MJ, Verdeja LF, Verdeja JI. Structural Ultrafine Grained Steels Obtained by Advanced Controlled Rolling. J Iron Steel Res Int. 2013;20:62–70. doi: 10.1016/S1006-706X(13)60046-1.
[33] Eberle A, Klingbeil D, Baer W, Wossidlo P, Häcker R. The calculation of dynamic JR-curves from 2D and 3D finite element analyses of a Charpy test using a rate-dependent damage model. Euro Struct Integr Soc. 2002;30:403–10. doi: 10.1016/S1566-1369(02)80045-0.
[34] Brüggemann JP, Risse L, Kullmer G, Schramm B, Richard HA. Fracture mechanical investigations on selective laser melted Ti-6Al-4V. Proc Struct Integr. 2018;13:317–21. doi: 10.1016/j.prostr.2018.12.053.

[35] Zou X, Lo SB, Sevilla R, Hassan O, Morgan K. The generation of 3D surface meshes for NURBS-enhanced FEM. Comput Aid Des. 2024;168:103653. doi: 10.1016/j.cad.2023.103653.
[36] Li X, Li X, Wu Y, Wu L, Yue Z. Selection criteria of mesh size and time step in FEM analysis of highly nonlinear unsaturated seepage process. Comput Geotech. 2022;146:104712. doi: 10.1016/j.compgeo.2022.104712.
[37] Su W, Qiu YY, Xu, Wang J. A scheme for switching boundary condition types in the integral static-dynamic analysis of soil-structures in Abaqus. Soil Dyn Earthq Eng. 2021;141:106458. doi: 10.1016/j.soildyn.2020.106458.
[38] Behtaaj M, Babaei H, Mostofi TM. Repeated uniform blast loading on welded mild steel rectangular plates. Thin Wall Struct. 2022;178:109523. doi: 10.1016/j.tws.2022.109523.
[39] Ghovehoud MR, Sarrami S, Azhari M, Shahmohammadi MA. Dynamic instability analysis of sandwich plates with auxetic honeycomb core and three-phase hybrid composite layers stiffened by curved stiffeners using isogeometric analysis. Eng Struct. 2024;308:117960. doi: 10.1016/j.engstruct.2024.117960.
[40] Beskou ND, Tsinopoulos SV, Theodorakopoulos DD. Dynamic elastic analysis of 3-D flexible pavements under moving vehicles. A unified FEM treatment. Soil Dyn Earthq Eng. 2016;82:63–72. doi: 10.1016/j.soildyn.2015.11.013.
[41] Xu Z. On multi-period multi-attribute decision making. Konwl Base Syst. 2008;21:164–71. doi: 10.1016/j.knosys.2007.05.007.
[42] Ihsanudin WN, Prabowo AR, Muhayat N, Adiputra R, Bahatmaka A, Baek SJ. Estimating hydrodynamic performances of the designed leisure boats: a study considering hull shape and dimension variations. Eng Res Expr. 2024;6(3):035506. doi: 10.1088/2631-8695/ad5c28.
[43] Pratama AS, Prabowo AR, Tuswan T, Adiputra R, Muhayat N, Cao B, et al. Fast patrol boat hull design concepts on hydrodynamic performances and survivability evaluation. J Appl Eng Sci. 2023;21(2):501–31. doi: 10.5937/jaes0-40698.
[44] Rahmaji T, Prabowo AR, Tuswan T, Muttaqie T, Muhayat N, Baek SJ. Design of fast patrol boat for improving resistance, stability, and seakeeping performance. Designs. 2022;6(6):105. doi: 10.3390/designs6060105.
[45] Diatmaja H, Prabowo AR, Adiputra R, Muhayat N, Baek SJ, Huda N, et al. Comparative evaluation of design variations in prototype fast boats: A hydrodynamic characteristic-based approach. Math Model Eng Probl. 2023;10(5):1487–507. doi: 10.18280/mmep.100501.
[46] Yusfianda AR, Diatmaja H, Prabowo AR, Tuswan T, Muttaqie T, Muhayat N, et al. Developing hull design based on the hydrodynamic criteria: An application for leisure boats as a tourist facility. Int J Mech Eng Robot Res. 2024;13(3):368–85. doi: 10.18178/ijmerr.13.3.368-385.
[47] Lutfi MA, Prabowo AR, Muslimy EM, Muttaqie T, Muhayat N, Diatmaja H, et al. Leisure boat concept design: study on the influence of hull form and dimension to increase hydrodynamic performance. Int J Mech Eng Robot Res. 2024;13(1):139–61. doi: 10.18178/ijmerr.13.1.139-161.
[48] Helvacioglu S, Ozen E. Fuzzy based failure modes and effect analysis for yacht system design. Ocean Eng. 2014;79:131–41. doi: 10.1016/j.oceaneng.2013.12.015.
[49] Rezasefat M, Ma D, da Silva AA, Colombo C, Amico SC, Giglio M, et al. Multi-criteria decision-making analysis and numerical simulation of the low-velocity impact response of inter-ply S2-glass/aramid woven fabric hybrid laminates. Compos Struct. 2023;312:116867. doi: 10.1016/j.compstruct.2023.116867.
[50] Hu H, Zuo Q, Li H, Yang K. Stochastic multi-attribute group decision-making for long-term comprehensive operation of cascade reservoirs under multiple uncertainties. J Hydrol Reg Stud. 2024;53:101758. doi: 10.1016/j.ejrh.2024.101758.
[51] Prabowo AR, Cao B, Sohn JM, Bae DM. Crashworthiness assessment of thin-walled double bottom tanker: Influences of seabed to structural damage and damage-energy formulae for grounding damage calculations. J Ocean Eng Sci. 2020;5(4):387–400. doi: 10.1016/j.joes.2020.03.002.
[52] Nisa AWS, Adiputra R, Prabowo AR, Kim DK, Sukanto H, Lutfi YM, et al. Forecasting the ultimate strength of designed thin-walled very large crude carrier class structures based on imperfection and pressure severities: Benchmarking and developing an empirical formula. Eng Sci. 2024;29:1096. doi: 10.30919/es1096.
[53] Prabowo AR, Ridwan R, Braun M, Song S, Ehlers S, Firdaus N, et al. Comparative study of shell element formulations as NLFE parameters to forecast structural crashworthiness. Curve Layer Struct. 2023;10(1):20220217. doi: 10.1515/cls-2022-0217.
[54] Prabowo AR, Ridwan R, Tuswan T, Smaradhana DF, Cao B, Baek SJ. Crushing resistance on the metal-based plate under impact loading: A systematic study on the indenter radius influence in grounding accident. Appl Eng Sci. 2024;18:100177. doi: 10.1016/j.apples.2024.100177.
[55] Nurcholis A, Prabowo AR, Muhayat N, Yaningsih I, Tjahjana DD, Jurkovič M, et al. Performances of the sandwich panel structures under fire accident due to hydrogen leaks: Consideration of structural design and environment factor using FE analysis. Curve Layer Struct. 2024;11(1):20240005. doi: 10.1515/cls-2024-0005.
[56] Prabowo AR, Bae DM, Sohn JM, Zakki AF. Evaluating the parameter influence in the event of a ship collision based on the finite element method approach. Int J Technol. 2016;7(4):592–602. doi: 10.14716/ijtech.v7i4.2104.